EUROPEAN ORGANISATION FOR NUCLEAR RESEARCH (CERN)

Submitted to: JHEP

CERN-EP-2022-026
6th May 2022

Differential $t\bar{t}$ cross-section measurements using boosted top quarks in the all-hadronic final state with 139 fb^{-1} of ATLAS data

The ATLAS Collaboration

Measurements of single-, double-, and triple-differential cross-sections are presented for boosted top-quark pair-production in 13 TeV proton–proton collisions recorded by the ATLAS detector at the LHC. The top quarks are observed through their hadronic decay and reconstructed as large-radius jets with the leading jet having transverse momentum (p_{T}) greater than 500 GeV. The observed data are unfolded to remove detector effects. The particle-level cross-section, multiplied by the $t\bar{t} \to WWb\bar{b}$ branching fraction and measured in a fiducial phase space defined by requiring the leading and second-leading jets to have $p_{\mathrm{T}} > 500$ GeV and $p_{\mathrm{T}} > 350$ GeV, respectively, is 331 ± 3(stat.) ± 39(syst.) fb. This is approximately 20% lower than the prediction of 398^{+48}_{-49} fb by Powheg+Pythia 8 with next-to-leading-order (NLO) accuracy but consistent within the theoretical uncertainties. Results are also presented at the parton level, where the effects of top-quark decay, parton showering, and hadronization are removed such that they can be compared with fixed-order next-to-next-to-leading-order (NNLO) calculations. The parton-level cross-section, measured in a fiducial phase space similar to that at particle level, is 1.94 ± 0.02(stat.) ± 0.25(syst.) pb. This agrees with the NNLO prediction of $1.96^{+0.02}_{-0.17}$ pb. Reasonable agreement with the differential cross-sections is found for most NLO models, while the NNLO calculations are generally in better agreement with the data. The differential cross-sections are interpreted using a Standard Model effective field-theory formalism and limits are set on Wilson coefficients of several four-fermion operators.

Contents

1 Introduction

The large top-quark pair-production cross-section at the Large Hadron Collider (LHC) results in high-statistics samples of top-quark–top-antiquark ($t\bar{t}$) pairs that enable unique tests of the Standard Model (SM) and searches for new phenomena that affect $t\bar{t}$ production. A focus on final states with highly boosted top quarks probes the QCD $t\bar{t}$ production processes at the TeV scale, a kinematic region where theoretical calculations based on the SM still have large uncertainties [1–3]. High-precision measurements constrain these predictions, especially at $t\bar{t}$ invariant masses of 2 TeV or more. Furthermore, effects beyond the SM may appear as deviations of $t\bar{t}$ differential distributions from the SM prediction [4–6].

In the SM, the top quark decays almost exclusively into a W boson and a b-quark. The signature of a $t\bar{t}$ final state is therefore determined by the W boson decay modes. The ATLAS [7–15] and CMS [16–27] collaborations have published measurements of the $t\bar{t}$ differential cross-sections at centre-of-mass energies of $\sqrt{s}$ = 7 TeV, 8 TeV, and 13 TeV in proton–proton (pp) collisions using final states containing leptons and jets, with most measurements employing the lepton+jets or dilepton channels. The analysis presented here makes use of the all-hadronic $t\bar{t}$ decay mode, where only top-quark candidates with high transverse momentum (p_{T}) being reconstructed as jets are selected. This highly boosted topology has advantages over other final states since the Lorentz boost of the top quark collimates its decay products such that they can be collected into a large-radius (large-R) jet. Although this final state has the largest branching ratio and the absence of neutrinos from W decays allows direct detection of all decay products, it is also less studied given the large backgrounds coming from multijet production [15, 26]. These features make measurements of the all-hadronic final state complementary to studies of the lepton+jets and dilepton channels.

This analysis is performed by targeting events where the leading top-quark jet has $p_{\mathrm{T}}^{t,1} > 500$ GeV and the second-leading top-quark jet has $p_{\mathrm{T}}^{t,2} > 350$ GeV. These jets are reconstructed from calorimeter energy deposits and tagged as top-quark candidates to separate the $t\bar{t}$ final state from background sources. The top-quark-tagging algorithm uses high-level jet-substructure information as input to a deep neural network (DNN) that efficiently discriminates between top-quark jets resulting from hadronic top-quark decay and the various backgrounds [28, 29]. Moreover, the jets containing b-hadrons coming from hadronization of b-quarks from top-quark decays are identified using another DNN that exploits information from large-impact-parameter tracks, the topological decay chain and the displaced vertices of b-hadron decays [30, 31]. The event selection and background estimation follows the approach used in Ref. [32], but with a fourfold increase in sample size, improved tagging methods [28–31, 33], and more precise background estimates.

These measurements utilise data collected by the ATLAS detector between 2015 and 2018 from pp collisions at $\sqrt{s}$ = 13 TeV, referred to as Run 2, corresponding to an integrated luminosity of 139 fb^{-1}. The $t\bar{t}$ differential cross-sections are measured by unfolding the detector-level distributions to a particle-level fiducial phase-space region and a parton-level fiducial phase-space region. The particle-level criteria intend to match the kinematic requirements used for the detector-level selection of the $t\bar{t}$ events while the parton-level region is defined by making the same cuts on the p_{T} of the leading and second-leading top quark as at the detector-level. Unfolding the observed distributions to distributions of variables directly related to the detector observables in a particle-level fiducial phase space allow for precision tests of QCD, as the particle-level results can be compared with Monte Carlo (MC) generator predictions that implement matrix-element calculations at next-to-leading order (NLO) in the strong coupling constant α_{s}, leading-order (LO) models for top-quark decay, and parton-shower and hadronization models. This procedure avoids model-dependent extrapolation of the measurements to a phase-space region outside the detector acceptance. The size of the phase space nonetheless is large enough to allow robust tests of

the QCD predictions. Parton-level differential cross-sections are also presented, where the detector-level distributions are unfolded to measure the top-quark kinematics at the parton level in a larger phase-space region, allowing measurement of the QCD process factoring out the parton showering and hadronization of the quarks and gluons. These allow comparisons with next-to-next-to-leading-order (NNLO) predictions for which matching to a parton-shower algorithm is not yet available. Here and in what follows, the cross-sections and distributions created using MC generators are referred to as calculations or predictions, while distributions created using MC events passed through the detector simulation and event reconstruction are referred to as simulations.

The modelling of differential cross-sections are affected by the models for initial- and final-state radiation (ISR and FSR), parton distribution functions (PDFs), and the scheme for matching matrix-element calculations to parton-shower models. Their measurement therefore tests the NLO QCD predictions for these aspects.

Measurements of the differential cross-sections for the leading and second-leading top quarks are made as a function of their p_{T} and rapidity y. In addition, the differential cross-sections for the transverse momentum (p_{T}^{t}) and absolute rapidity ($|y^{t}|$) of a top quark chosen at random from the event are measured. These are equivalent to the average of the top-quark and top-antiquark distributions and are typically easier to compare with fixed-order predictions and measurements in other channels than kinematic distributions of the leading or second-leading jet. The rapidities of the leading and second-leading top quarks in the laboratory frame are denoted by $y^{t,1}$ and $y^{t,2}$, respectively, while their rapidities in the $t\bar{t}$ centre-of-mass frame are $y^{\star} = 1/2\left(y^{t,1} - y^{t,2}\right)$ and $-y^{\star}$. These allow the construction of the observable $\chi^{t\bar{t}} = \exp(2|y^{\star}|)$, which is of particular interest since many phenomena not included in the SM, such as quark substructure, are predicted to peak at low values of $\chi^{t\bar{t}}$ [34]. The longitudinal motion of the $t\bar{t}$ system in the laboratory frame is described by the rapidity boost $y_{\mathrm{B}}^{t\bar{t}} = 1/2\left(y^{t,1} + y^{t,2}\right)$ and is sensitive to PDFs. The unfolded distributions for the $t\bar{t}$ invariant mass ($m^{t\bar{t}}$), transverse momentum ($p_{\mathrm{T}}^{t\bar{t}}$), and absolute value of rapidity ($\left|y^{t\bar{t}}\right|$) are constructed, as these test QCD predictions and are sensitive to processes beyond the SM (BSM processes). Measurements of the differential cross-sections are also performed as a function of the absolute value of the azimuthal angle between the two top quarks, $\left|\Delta\phi^{t\bar{t}}\right|$; the absolute value of the out-of-plane momentum, $\left|p_{\mathrm{out}}^{t\bar{t}}\right|$ (i.e. the projection of the three-momentum of the second-leading top quark onto the direction perpendicular to a plane defined by the leading top quark and the beam axis (z) in the laboratory frame [35]); the cosine of the production angle in the Collins–Soper reference frame [36], $\cos\theta^{\star}$; and the scalar sum of the transverse momenta of the two top quarks, $H_{\mathrm{T}}^{t\bar{t}}$ [37, 38]. Several double- and triple-differential cross-sections employing pairs and triplets of these observables are measured to provide information about correlations. These are particularly sensitive to QCD modelling and have been shown to constrain PDFs [20, 25].

These measurements are compared with different QCD predictions. Direct comparisons of the differential cross-sections incorporating statistical and systematic uncertainties identify the predictions that are in best agreement with the data. Measurements unfolded to the particle-level fiducial phase space and parton-level fiducial phase space are compared with QCD predictions at NLO produced by the Powheg Box v2 [39–42] and MadGraph5_aMC@NLO [43] programs. Measurements unfolded to the parton-level fiducial phase space are compared with a NNLO calculation implemented in the Matrix program [44–46]. Other NNLO calculations for $t\bar{t}$ production exist [1, 47–49] but are not publicly available to make predictions in the phase space and/or final state employed in these measurements.

The unfolded distributions are also used to set constraints on the magnitude of particle couplings beyond the SM using the SM effective field theory (SMEFT) that extends the SM by adding higher-order dimension

operators suppressed by the scale of the new physics that respect the Lorentz and gauge invariance and other assumed basic symmetries [50]. Using a LO SMEFT model that incorporates a full list of dimension-6 operators involved in top-quark interactions [51], limits are set on a subset of Wilson coefficients and on selected pairs of these coefficients. These can be related to the couplings and production of massive particles beyond the SM.

The paper is organized as follows. Section 2 describes the ATLAS detector, while Section 3 describes the data and simulation samples used in the measurements. The reconstruction of lepton and jet candidates, and the event selection based on these, is explained in Section 4 and the background estimates are discussed in Section 5. The detector-level results are presented in Section 6. The procedure for particle-level and parton-level unfolding is described in Section 7. The systematic uncertainties affecting the measurements are summarized in Section 8. The results of the measurements are presented in Section 9 and comparisons of these results with theoretical predictions are made in Section 10. The results of the analysis using the SMEFT formalism are presented in Section 11. Conclusions of this study are summarized in Section 12.

2 ATLAS detector

The ATLAS detector [52] at the LHC covers nearly the entire solid angle around the collision point.[1] It consists of an inner tracking detector surrounded by a thin superconducting solenoid, electromagnetic and hadron calorimeters, and a muon spectrometer incorporating large superconducting air-core toroidal magnets.

The inner-detector system (ID) is immersed in a 2 T axial magnetic field and provides charged-particle tracking in the range $|\eta| < 2.5$. The high-granularity silicon pixel detector covers the vertex region and typically provides four measurements per track, the first hit normally being in the insertable B-layer installed before Run 2 [53, 54]. It is followed by the silicon microstrip tracker, which usually provides eight measurements per track. These silicon detectors are complemented by the transition radiation tracker, which enables radially extended track reconstruction up to $|\eta| = 2.0$.

The calorimeter system covers the pseudorapidity range $|\eta| < 4.9$. Within the region $|\eta| < 3.2$, electromagnetic calorimetry is provided by barrel and endcap high-granularity lead/liquid-argon (LAr) calorimeters, with an additional thin LAr presampler covering $|\eta| < 1.8$ to correct for energy loss in material upstream of the calorimeters. Hadron calorimetry is provided by the steel/scintillator-tile calorimeter, segmented into three barrel structures within $|\eta| < 1.7$, and two copper/LAr hadron endcap calorimeters. The solid angle coverage is completed with forward copper/LAr and tungsten/LAr calorimeter modules optimized for electromagnetic and hadronic energy measurements, respectively.

The muon spectrometer (MS) comprises separate trigger and high-precision tracking chambers measuring the deflection of muons in a magnetic field generated by the superconducting air-core toroidal magnets. The field integral of the toroids ranges between 2.0 and 6.0 T m across most of the detector. A set of precision chambers covers the region $|\eta| < 2.7$ with three layers of monitored drift tubes, complemented by cathode-strip chambers in the forward region, where the background is highest. The muon trigger system

[1] ATLAS uses a right-handed coordinate system with its origin at the nominal interaction point (IP) in the centre of the detector and the z-axis along the beam pipe. The x-axis points from the IP to the centre of the LHC ring, and the y-axis points upwards. Cylindrical coordinates (r, ϕ) are used in the transverse plane, ϕ being the azimuthal angle around the z-axis. The pseudorapidity is defined in terms of the polar angle θ as $\eta = -\ln\tan(\theta/2)$. Angular distance is measured in units of $\Delta R \equiv \sqrt{(\Delta\eta)^2 + (\Delta\phi)^2}$.

covers the range $|\eta| < 2.4$ with resistive-plate chambers in the barrel, and thin-gap chambers in the endcap regions.

Interesting events are selected by the first-level trigger system implemented in custom hardware, followed by selections made by algorithms implemented in software in the high-level trigger [55]. The first-level trigger accepts events from the 40 MHz bunch crossings at a rate below 100 kHz, which the high-level trigger further reduces in order to record events to disk at about 1 kHz. An extensive software suite [56] is used in the reconstruction and analysis of real and simulated data, in detector operations, and in the trigger and data acquisition systems of the experiment.

3 Data and simulated event samples

The data used for this analysis were recorded with the ATLAS detector at a pp centre-of-mass energy of 13 TeV between 2015 and 2018 and correspond to an integrated luminosity of 139 fb^{-1}. Only data taken under stable beam conditions with fully operational subdetectors are considered [57]. The events for this analysis were collected using an inclusive jet trigger employing anti-k_t [58] reconstruction with radius parameter $R = 1.0$ and nominal p_{T} thresholds of 360 GeV in 2015, 420 GeV in 2016, and 460 GeV in 2017 and 2018. Moreover, single-jet and double-jet triggers with lower p_{T} thresholds and jet-mass requirements of >40 GeV and >35 GeV were used in 2017 and 2018, respectively. These triggers are fully efficient for jets with $p_{\mathrm{T}} > 500$ GeV [55].

The signal and several background processes were modelled using MC generators. The effect of multiple interactions in the same and neighbouring bunch crossings (pile-up) was modelled by overlaying the simulated hard-scattering event with inelastic pp events generated with Pythia 8 [59] using the NNPDF2.3lo set of PDFs [60] and the A3 set of tuned parameters [61]. The detector response was simulated using the Geant4 framework [62, 63]. The data and MC events are reconstructed with the same software algorithms.

Several NLO calculations of the $t\bar{t}$ process are used to generate the simulated events and in comparisons with the measured differential cross-sections. The Powheg Box v2 [39–42] and MadGraph5_aMC@NLO [43] (hereafter referred to as aMC@NLO) MC generators encode different approaches to the matrix-element calculation and different matching schemes between the NLO QCD matrix-element (ME) calculation and the parton-shower (PS) algorithm. Unless explicitly noted below, the following generator set-ups were used. The employed PDF set is NNPDF3.0nlo [64]. Parton showering and hadronization was performed with Pythia 8.230 [65] using the A14 set of tuned parameters [66] and the NNPDF2.3lo set of PDFs. The top-quark mass was set to $m_{\mathrm{top}} = 172.5$ GeV for all samples with the top quark in the final state and the renormalization and factorization scales were set to $\mu_{\mathrm{r/f}} = \sqrt{m_{\mathrm{top}}^2 + p_{\mathrm{T}}^2}$ for all $t\bar{t}$ samples, where p_{T} is the transverse momentum of the top quark. The decays of bottom and charm hadrons were simulated using the EvtGen 1.6.0 program [67].

The nominal sample used the Powheg Box v2 generator at NLO in QCD. The h_{damp} parameter, which controls the matching in the Powheg calculation and effectively regulates the high-p_{T} radiation against which the $t\bar{t}$ system recoils, was set to $1.5\, m_{\mathrm{top}}$ [68]. To increase the available statistics for events with high-p_{T} top quarks, multiple samples were generated with different ranges of the total scalar sum of p_{T} in the event.

An alternative Powheg+Pythia 8 sample with the Powheg parameter h_{damp} set to $3m_{\text{top}}$ was used to assess part of the ISR systematic uncertainty [69]. An additional Powheg+Pythia 8 sample was generated with the matrix-element correction turned off in order to assess the systematic uncertainty due to this change in the matrix-element calculation.

An alternative matrix-element calculation and matching with the parton shower was realized with the aMC@NLO 2.6.0 generator. Top quarks were decayed at LO using the MadSpin program [70, 71] to preserve spin correlations. The parton-shower starting scale has the functional form $\mu_{\text{q}} = H_{\text{T}}/2$ [72], where H_{T} is defined as the scalar sum of the p_{T} of all outgoing partons.

The effects of using alternative parton-shower and hadronization models were probed by combining the nominal Powheg set-up with the Herwig 7.1.3 parton-shower and hadronization model [73, 74], using the Herwig 7.1 default set of tuned parameters [74, 75] and the MMHT2014lo PDF set [76].

Single-top-quark production in association with a W boson (tW) was modelled by the Powheg Box v2 generator at NLO using the five-flavour scheme. The diagram-removal scheme [77] was used to remove interference and overlap with $t\bar{t}$ production. Electroweak t-channel single-top-quark events were modelled using Powheg Box v2 [78] at NLO in the four-flavour scheme. The electroweak s-channel single-top-quark process was not modelled explicitly, owing to its small cross-section and the low jet multiplicity in the final state. Its contribution is accounted for in the data-driven background estimate. The decays of bottom and charm hadrons were simulated using the EvtGen 1.2.0 program.

The associated production of $t\bar{t}$ and a Higgs boson ($t\bar{t}H$) was modelled by the Powheg Box v2 [79] generator at NLO. The associated production of $t\bar{t}$ and a W or Z boson ($t\bar{t}V$) was modelled using the aMC@NLO 2.3.3 generator at NLO. Parton showering and hadronization was performed by the Pythia 8.210 generator. The decays of bottom and charm hadrons were simulated using the EvtGen 1.2.0 program.

The $t\bar{t}$ samples are normalized to the cross-section prediction at NNLO in QCD including the resummation of next-to-next-to-leading logarithmic (NNLL) soft-gluon terms calculated using the Top++ 2.0 program [80–86]. For pp collisions at a centre-of-mass energy of $\sqrt{s} = 13\,\text{TeV}$, this cross-section corresponds to $\sigma(t\bar{t})_{\text{NNLO+NNLL}} = 832 \pm 51\,\text{pb}$ using a top-quark mass of $m_{\text{top}} = 172.5\,\text{GeV}$. The uncertainties in the cross-section due to the PDFs and α_{s} are calculated using the PDF4LHC15 prescription [87] with the MSTW2008nnlo [88, 89], CT10nnlo [90, 91], and NNPDF2.3lo PDF sets in the five-flavour scheme, and are added in quadrature to the effect of the scale uncertainty.

Calculations of $t\bar{t}$ production at NNLO matched to the parton shower to produce particle-level predictions are not yet available for the all-hadronic final state. In order to evaluate the impact of NNLO corrections, the MC set-ups are reweighted at parton level. The reweighting is performed on the three variables: p_{T}^{t}, $m^{t\bar{t}}$, and $p_{\text{T}}^{t\bar{t}}$, using the kinematics of the top-quarks in the MC samples after ISR and FSR. The predictions for p_{T}^{t} and $m^{t\bar{t}}$ are calculated at NNLO in QCD with NLO EW corrections [1] with the NNPDF3.0QED PDF set using the dynamic renormalisation and factorisation scales $m_{\text{T}}(t)/2$ for p_{T}^{t} and $H_{\text{T}}^{t\bar{t}}/4$ for $m^{t\bar{t}}$ as proposed in Ref. [1]. The prediction for $p_{\text{T}}^{t\bar{t}}$ is calculated at NNLO in QCD [44–46] with the NNPDF3.0 PDF set using renormalisation and factorisation scales $H_{\text{T}}^{t\bar{t}}/4$. All the predictions use $m_{\text{top}} = 173.3\,\text{GeV}$. The reweighting has been derived iteratively [92], such that at the end of the procedure the reweighted MC sample is in good agreement with the high-order prediction for each of the three variables. These samples are referred to as being reweighted to the NNLO prediction in the remainder of the paper.

The single-top-quark tW cross-section is normalized to the calculation at NLO with NNLL soft-gluon corrections [93, 94]. The single-top-quark t-channel cross-section is normalized to the NLO calculation with the Hathor 2.1 program [95, 96]. The predicted values at $\sqrt{s} = 13\,\text{TeV}$ are $136.02^{+5.40}_{-4.57}\,\text{pb}$, $80.95^{+4.06}_{-3.61}\,\text{pb}$,

and 71.7 ± 3.8 pb for t-channel top-quark production, t-channel top-antiquark production, and tW production, respectively. The cross-sections for $t\bar{t}$ production in association with a Z, W, or Higgs boson are normalized to the NLO QCD + NLO electroweak predictions as calculated by the aMC@NLO generator and reported in Ref. [97]. The predicted values at $\sqrt{s} = 13$ TeV are $0.88^{+0.09}_{-0.11}$ pb, $0.60^{+0.08}_{-0.07}$ pb, and $0.51^{+0.04}_{-0.05}$ pb, respectively.

Comparisons with the measured differential cross-sections at parton level use a calculation of $t\bar{t}$ production at QCD NNLO precision by the Matrix program [44–46], which provides differential $t\bar{t}$ predictions in the full and fiducial phase space. For the nominal Matrix prediction, the NNPDF3.1nnlo PDFs are employed with $\alpha_s(m_Z) = 0.118$ set in the calculations [98], together with renormalization and factorization dynamical scales of $\mu_r = \mu_f = H_T/2$, where $H_T = \sqrt{m_{top}^2 + p_{T,t}^2} + \sqrt{m_{top}^2 + p_{T,\bar{t}}^2}$. For the alternative predictions, the dynamical scales are defined by $\mu_r = \mu_f = H_T/4$ and $\mu_r = \mu_f = m_{t\bar{t}}/2$, and the CT18nnlo [99] and MMHT2014nnlo [76] PDFs are used. A seven-point scale variation is used to obtain the effect of the scale uncertainty by varying the renormalization and factorization scales by a factor of two around their central value with the constraint $0.5 \leq \mu_f/\mu_r \leq 2$. The largest upward and downward changes from the central-value result are taken as positive and negative uncertainties, respectively.

4 Selection of events

Fully reconstructed and individually selected jets, electrons, and muons, together with selections on the final-state topology measured with those, are used when choosing the events considered for this analysis. The applied selection criteria are summarized in the following subsections.

4.1 Particle and jet selections

Electron candidates are identified from high-quality ID tracks matched to calorimeter energy deposits consistent with an electromagnetic shower. The energy deposits have to form a cluster with $p_T > 25$ GeV and $|\eta| < 2.47$, and be outside the transition region $1.37 \leq |\eta| \leq 1.52$ between the barrel and endcap calorimeters. A tight likelihood-based requirement is used to reject fake-electron candidates, and calorimeter- and track-based isolation requirements are imposed [100].

Muon candidates are reconstructed using high-quality inner-detector tracks combined with tracks reconstructed in the muon spectrometer. Only muon candidates satisfying 'medium' identification criteria [101], with $p_T > 25$ GeV and $|\eta| < 2.5$, are considered. Isolation criteria similar to those used for electrons are imposed [101]. To reduce the impact of non-prompt leptons, muons within $\Delta R = 0.4$ of a small-R jet, as defined below, are removed.

The anti-k_t [58] and variable-R [102] algorithms implemented in the FastJet package [103] are used to define three types of jets for this analysis: large-R jets with fixed $R = 1.0$ [104], small-R jets with fixed $R = 0.4$ used to investigate the internal kinematics of the large-R jets, and variable-R jets with a p_T-dependent variable-radius parameter, ranging between $R = 0.02$ and $R = 0.4$ [102, 105], which are used to identify b-hadrons. These are reconstructed independently of each other. The large-R jets are formed from topological clusters in the calorimeter calibrated using the local calibration method described in Ref. [106], while the small-R jets are reconstructed from both calorimeter energy clusters and charged-particle tracks. The variable-R jets are reconstructed from inner-detector tracks that are

used as input to the clustering algorithm. Only variable-R jets that have $|\eta| < 2.5$ and $p_{\mathrm{T}} > 10$ GeV are considered. Small-R jets with $p_{\mathrm{T}} < 60$ GeV are required to have charged-particle tracks matched to the primary interaction vertex [107].

Variable-R jets containing b-hadrons are identified (b-tagged) using a DNN that exploits information from large-impact-parameter tracks, the topological decay chain and the displaced vertices of b-hadron decays [30, 31]. The variable-R jets are considered b-tagged if the value of the discriminant is larger than a threshold that provides 77% efficiency as measured in inclusive $t\bar{t}$ events. The b-tagging efficiency observed in the boosted top-quark jets employed in this analysis is found to be ~70%, which arises from the increased collimation and charged-particle track density in the top-quark jets. The corresponding rejection factors for gluon/light-quark jets and charm-quark jets are approximately 300 and 7, respectively, as measured in inclusive $t\bar{t}$ events. The variable-R jets are associated with the large-R jets using a ghost-matching algorithm [108, 109], which identifies those variable-R jets that are contained within or are in proximity to the large-R jet. A large-R jet with at least one associated b-tagged variable-R jet is considered b-tagged.

The large-R and small-R jet energy and mass scales are corrected by using energy- and η-dependent calibration factors derived from simulation and in situ measurements [110, 111]. The large-R jet candidates are required to have $|\eta| < 2.0$, 200 GeV $< p_{\mathrm{T}} <$ 3000 GeV, and jet mass >50 GeV, where η is used instead of rapidity for selection at the detector level because the jet calibrations were determined as a function of η. A trimming algorithm [112] with parameters $R_{\mathrm{sub}} = 0.2$ and $f_{\mathrm{cut}} = 0.05$ is applied to the large-R jets to suppress gluon radiation and mitigate pile-up effects.

The top-quark tagging of large-R jets relies on a DNN that uses jet-substructure variables such as the jet mass and measures of energy flow as input [28, 29]. The p_{T}-dependent requirements on the DNN score provide 80% top-quark-tagging efficiency, as measured in inclusive $t\bar{t}$ events where the top-quark decay products are contained within the large-R jet. The tagging efficiency for top-quark jets with $p_{\mathrm{T}} > 500$ GeV falls to ~70% due to the collimation of the particles in the jets. The algorithm has a light-quark and gluon jet-rejection factor that is p_{T}-dependent, being ~40 at $p_{\mathrm{T}} = 500$ GeV and decreasing to ~ 15 at $p_{\mathrm{T}} = 1$ TeV, as measured in multijet events.

4.2 Event selection

The event selection targets fully hadronic $t\bar{t}$ events where both top-quark jets have high p_{T}. Each event is required to have a primary vertex with at least two associated ID tracks with $p_{\mathrm{T}} > 0.5$ GeV. The vertex with the highest $\sum p_{\mathrm{T}}^2$ of the associated tracks is taken as the primary vertex. In order to reject top-quark events where a top quark has decayed semileptonically, the events are required to contain no reconstructed electron or muon candidates. To identify the fully hadronic decay topology, events must have at least two large-R jets with $p_{\mathrm{T}} > 350$ GeV, with at least one of these having $p_{\mathrm{T}} > 500$ GeV. The first top-quark-candidate jet is selected among all the large-R jets with $p_{\mathrm{T}} > 500$ GeV as that with the closest mass to the nominal top-quark mass of 172.5 GeV. The second top-quark-candidate jet is selected from the remaining large-R jets with $p_{\mathrm{T}} > 350$ GeV, using the same mass requirement. Both top-quark-candidate jets must have a mass within 50 GeV of the top-quark mass. This preselection results in a sample of 2.2 million events.

To reject multijet background events, the two top-quark-candidate jets must satisfy the top-quark-tagging criteria described in Section 4.1 and must be b-tagged. The final-state $t\bar{t}$ candidate's momentum is defined by the sum of the four-momenta of the two top-quark-candidate jets.

This selection defines the signal region, which has 17 261 events.

2nd large-R jet \ Leading large-R jet	0t0b	1t0b	0t1b	1t1b
1t1b	J (10%)	K (29%)	L (45%)	S
0t1b	B (1.9%)	D (6.6%)	H (12%)	N (56%)
1t0b	E (0.7%)	F (2.7%)	G (5.9%)	M (35%)
0t0b	A (0.1%)	C (0.7%)	I (1.6%)	O (12%)

Table 1: Region labels and the fraction of $t\bar{t}$ events predicted by the nominal MC simulations in the region relative to the observed yield. A top-quark-tagged jet is defined by the tagging algorithm described in Section 4.1, and denoted by '1t' in the table, while a jet that is not top-quark-tagged is labelled '0t'. Jets that are or are not b-tagged are denoted by '1b' or '0b', respectively. The expected proportion of $t\bar{t}$ signal events and MC-predicted background events relative to the number of data events in each region is given in parentheses.

5 Background estimation

The backgrounds in the selected data sample are events characterized by a number of high-p_{T} jets that do not arise from a top quark, and events that have at least one top quark decaying semileptonically, have only one top quark decaying hadronically, or arise from production of a top-quark pair in association with a W, Z, or Higgs boson. The first contribution, referred to as multijet background and where the two leading jets both arise from gluons or lighter quarks, is found to be the largest background. Because the uncertainties in MC predictions of this background are large [113, 114], it is estimated using a data-driven approach. A similar method was used in previous work [15, 32]. The second set of contributions are from processes that can be relatively accurately calculated and simulated, and so MC calculations are used to estimate them.

The estimation of backgrounds from these sources is described in the following subsections.

5.1 Multijet background

The data-driven multijet-background estimate is made using a set of control regions. Sixteen separate regions are defined by classifying each event in the preselection sample according to whether the leading and second-leading jets are top-quark-tagged or b-tagged. Table 1 shows the 16 regions that are defined in this way, and indicates the expected proportion of $t\bar{t}$ signal events and MC-predicted background events relative to the number of data events in each region. These fractions illustrate the size of the MC-predicted subtractions in each region when calculating the data-driven multijet-background estimates. Region S is the signal region, while the regions with at most two tags that are either top-tags or b-tags (A–J, O) are dominated by multijet background and serve as control regions. Regions with three tags (K, L, N and M) have an expected contribution from top-quark pairs of at least 20% of the observed yield and are validation regions. In other regions, the expected contribution from signal and MC-predicted backgrounds is <10% of the number of observed events.

The estimated contributions of the $t\bar{t}$ signal and the MC-predicted backgrounds are subtracted from each control region, ignoring the small s-channel single-top-quark contribution and other small backgrounds. This provides an estimate of the number of multijet events in each control region. The number of multijet events in region J divided by the number of multijet events in region A gives an estimate of the ratio of the number of multijet events in region S to the number of multijet events in region O, since the events in different regions in a given ratio always differ only by the top-quark-tagging and b-tagging state of the

second-leading large-R jet. These relationships are used to estimate the multijet-background rate in region S, i.e. $S = (O \times J)/A$, where O, J and A are the number of multijet events in each region, while S is the estimate of the number of multijet background events in region S.

This 'ABCD' estimate assumes that the mistagging rate of the leading jet does not depend on how the second-leading jet is tagged, but in practice there are correlations between the mistagging rates of the two large-R jet candidates. These correlations are measured in the background-dominated regions, e.g. a comparison the ratio of the numbers of events in regions F and E (representing the leading-jet top-quark-mistagging rate when the second-leading jet is top-quark-tagged) with the ratio of the numbers of events in regions C and A (giving the leading-jet top-quark-mistagging rate when the second-leading jet is not top-quark-tagged) gives the correction factor due to the correlation between top-quark-mistagging states of the two large-R jets. This results in a data-driven estimate of the number of multijet background events in region S given by

$$\begin{aligned} S &= \frac{J \times O}{A} \cdot \frac{D \times A}{B \times C} \cdot \frac{G \times A}{E \times I} \cdot \frac{F \times A}{E \times C} \cdot \frac{H \times A}{B \times I} \\ &= \frac{J \times O \times H \times F \times D \times G \times A^3}{(B \times E \times C \times I)^2}, \end{aligned} \tag{1}$$

where the italic letters again represent the number of observed events in that region after the subtraction of $t\bar{t}$ signal events and the MC-predicted background events. The measured correlations result in a ~15% increase in the multijet estimate relative to the estimate assuming uncorrelated mistagging rates.

This background estimate depends on the assumed inclusive $t\bar{t}$ cross-section, which is the NNLO+NNLL cross-section prediction described in Section 3. However, it was found that even a 20% change in the assumed inclusive $t\bar{t}$ cross-section would cause only ~1% change in the measured fiducial phase-space $t\bar{t}$ cross-section, which is negligible compared to the uncertainty of the measurement.

This background estimate, including the mistagging correlations, is made bin-by-bin in the observed distributions. The statistical uncertainties reflect the number of events found in the regions used in Eq. (1) for each bin.

5.2 Non-all-hadronic $t\bar{t}$ background

The Powheg+Pythia 8 $t\bar{t}$ sample described in Section 3 is used to estimate the number of $t\bar{t}$ events in the sample that arise from at least one top quark decaying semileptonically. This estimate includes contributions from decays resulting in τ-leptons, as no attempt is made to identify τ-lepton candidates and reject them.

The proportion of this non-all-hadronic $t\bar{t}$ background is estimated to be only ~3% in the signal region, primarily due to the lepton-veto requirement in the preselection and the top-quark-tagging requirements. However, these $t\bar{t}$ events contribute to a greater degree to the control and validation regions, where the top-quark-tagging and/or b-tagging requirements are relaxed. A MC prediction is used to estimate the contributions to these regions, which therefore affects the multijet-background estimate. Although the $t\bar{t}$ production cross-section in the signal region is observed to be lower than the MC prediction, the use of a cross-section scaled to the signal region produces a negligible change in the multijet-background estimate.

5.3 Backgrounds from other top-quark production processes

Single-top-quark production in the Wt- and t-channel makes a small contribution to the signal sample, which is estimated using the MC predictions described in Section 3. The s-channel single-top-quark process is not explicitly calculated given its expected small contribution and its inclusion in the multijet-background estimate.

Backgrounds from a top-quark pair produced in association with a W, Z, or Higgs boson are estimated using the MC predictions also described in Section 3.

The cumulative background from these processes is ~2% in the signal region.

5.4 Validation of background calculations

The multijet-background estimate is validated using four validation regions, each with a different ratio of all-hadronic $t\bar{t}$ events to multijet events. In all these validation regions, the predicted $t\bar{t}$ contribution was scaled by the same factor of 0.83, obtained by scaling the $t\bar{t}$ contribution to match the total yield prediction to the data in the signal region. Regions L and N are estimated to consist of approximately equal numbers of $t\bar{t}$ signal events and multijet-background events while regions K and M are estimated to have a 2:1 ratio of multijet to $t\bar{t}$ events. In these regions, the multijet background is estimated using different combinations of control regions along with different corrections for the mistagging correlations.

The number of multijet events in the signal region is calculated by applying Eq. (1) to the number of events in the control regions. This results in an estimate of 2900 ± 160 multijet events in the signal region, where the uncertainty takes into account the data statistical uncertainties in the signal and control regions as well as the systematic uncertainties in the MC-based subtraction of top-quark-related contributions in the regions used in Eq. (1).

The ratios of predicted to observed yields in regions K, L, M, and N are 1.03, 0.99, 1.02, and 0.98, respectively, illustrating good agreement between the predicted and observed event yields in these validation regions within statistical and detector-related systematic uncertainties.

Good agreement between the distribution shapes is illustrated in Figures 1 and 2, which compare the mass distributions of the highest-p_{T} small-R jet associated with the leading and second-leading large-R jet, and the leading and second-leading large-R jet-mass distributions, for events in the signal region and in region L, where the leading jet is not top-quark-tagged but is b-tagged, while the second-leading jet is both top-quark-tagged and b-tagged. The small-R and large-R jets are considered to be associated if the angular separation between the small-R and large-R jet axes satisfies $\Delta R < 1.0$. The distributions of the leading-jet p_{T} and rapidity in regions N and L are shown in Figure 3. The predictions are in good agreement with the data distributions. Similar studies of validation regions with varying correlations between tagging states demonstrate that the multijet-background estimates are robust. These distributions can also be compared with the signal-region distributions in Figure 4, which illustrates the difference in the kinematics of the leading and second-leading large-R jets.

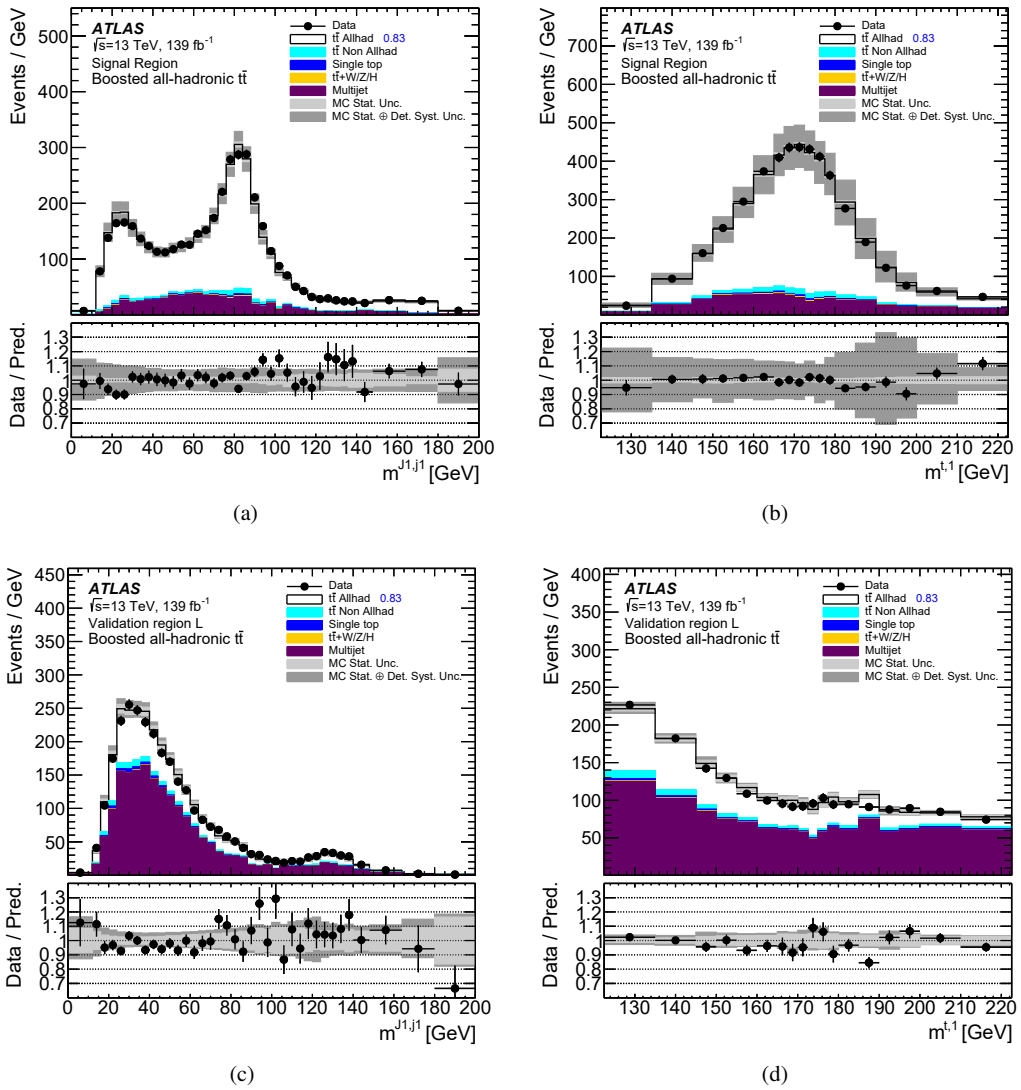

Figure 1: Kinematic distributions of the leading top-quark-candidate jets in the signal region and validation region L. The mass distributions of the leading $R = 0.4$ anti-k_t jet in the leading large-R jet for events in the signal region and region L are shown in (a) and (c), respectively. The leading large-R jet-mass distributions for the events in the signal region and validation region L are shown in (b) and (d), respectively. The signal prediction (open histogram) is based on the POWHEG+PYTHIA 8 $t\bar{t}$ calculation normalized to the observed yield in the signal region. The background (solid histogram) is the sum of the data-driven multijet estimate and the MC-based expectation for the non-all-hadronic $t\bar{t}$, single-top-quark, and $t\bar{t}+W/Z/H$ processes. The light grey bands indicate the statistical uncertainties and the dark grey bands indicate the combined statistical and detector-related systematic uncertainties defined in Section 8.

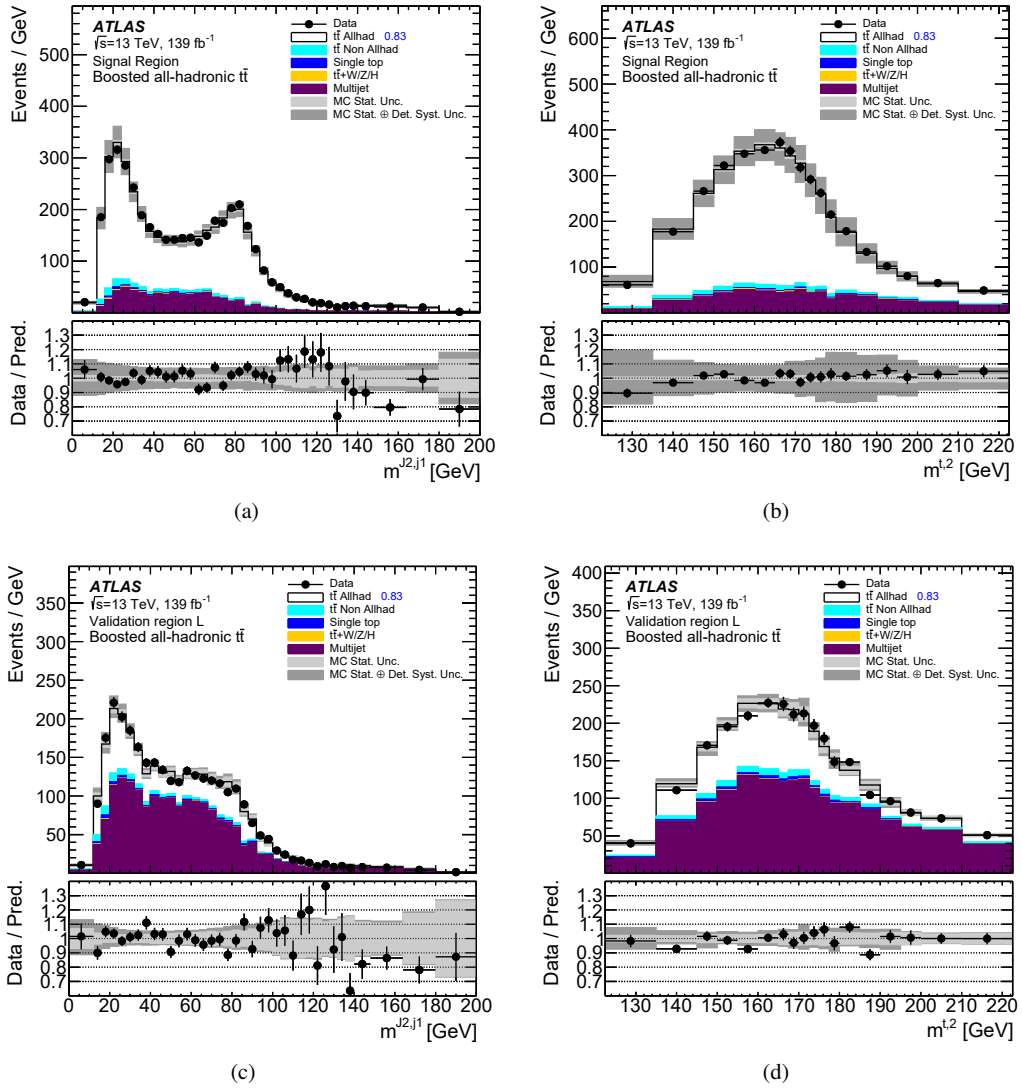

Figure 2: Kinematic distributions of the second-leading top-quark-candidate jets in the signal region and validation region L. The mass distributions of the leading $R = 0.4$ anti-k_t jet in the second-leading large-R jet for events in the signal region and region L are shown in (a) and (c), respectively. The second-leading large-R jet-mass distributions for the events in the signal region and validation region L are shown in (b) and (d), respectively. The signal prediction (open histogram) is based on the POWHEG+PYTHIA 8 $t\bar{t}$ calculation normalized to the observed yield in the signal region. The background (solid histogram) is the sum of the data-driven multijet estimate and the MC-based expectation for the contributions of non-all-hadronic $t\bar{t}$, single-top-quark, and $t\bar{t}+W/Z/H$ processes. The light grey bands indicate the statistical uncertainties and the dark grey bands indicate the combined statistical and detector-related systematic uncertainties defined in Section 8.

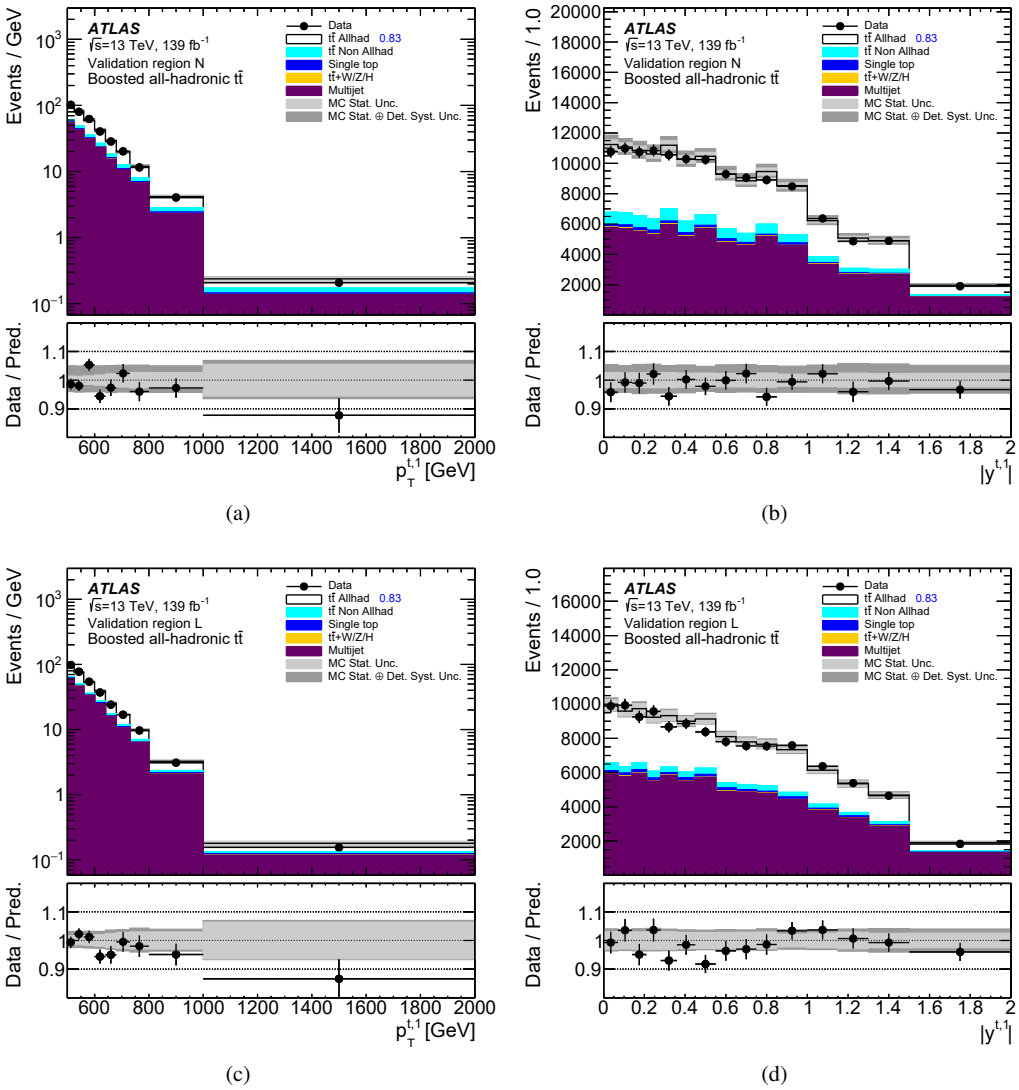

Figure 3: Kinematic distributions of the leading top-quark-candidate jets in validation regions N and L: (a) and (b) are distributions of the leading large-R jet p_{T} and the absolute value of the rapidity in region N, respectively, and (c) and (d) are the distributions of the leading large-R jet p_{T} and absolute value of the rapidity in region L. The signal prediction (open histogram) is based on the Powheg+Pythia 8 $t\bar{t}$ calculation normalized to the observed yield in a signal region. The background (solid histogram) is the sum of the data-driven multijet estimate and the MC-based expectation for the contributions of non-all-hadronic $t\bar{t}$, single-top-quark, and $t\bar{t}+W/Z/H$ processes. The light grey bands indicate the statistical uncertainties and the dark grey bands indicate the combined statistical and detector-related systematic uncertainties defined in Section 8.

Source	Event Yields
$t\bar{t}$ (all-hadronic)	16 200 ± 1400
$t\bar{t}$ (non-all-hadronic)	625 ± 63
Single top-quarks	179 ± 21
$t\bar{t}+W/Z/H$	114 ± 11
Multijet events	2900 ± 160
All Backgrounds	3820 ± 200
Prediction	20 000 ± 1600
Data (139 fb^{-1})	17 261

Table 2: Event yields in the signal region for the expected $t\bar{t}$ signal process and the background processes. The sum of these is compared with the observed yield. The uncertainties represent the sum in quadrature of the statistical and systematic uncertainties for each process, as described in Section 8. Neither $t\bar{t}$ modelling uncertainties nor uncertainties in the inclusive $t\bar{t}$ cross-section are included in the systematic uncertainties. The multijet-background uncertainty includes the statistical uncertainties in the signal and control regions as well as the systematic uncertainties arising from the MC-based subtraction in the control regions used to make the data-driven estimate. The column entries do not add up exactly to 'All Backgrounds' and 'Prediction' due to rounding.

6 Detector-level results

The event yields in the signal region are summarized in Table 2 for the simulated signal, the background sources, and the data sample. The prediction overestimates the data by about 16%. The systematic uncertainties apart from signal-modelling uncertainties, as described in detail in Section 8, are included in the prediction.

The comparisons between predicted and observed distributions in the signal region are shown in Figures 4 and Figure 5. Here, the $t\bar{t}$ MC prediction is scaled by requiring that the predicted and observed event yields match. The event yield decreases rapidly with increasing p_{T} of the leading and second-leading jets, which extends beyond 1 TeV, while the rapidity distributions fall slowly across the interval $|y| < 2.0$, as shown in Figure 4. Good agreement between the observed and predicted distributions also can be seen in Figure 4. In the signal region, the maximum observed p_{T} of the leading jet is 1.73 TeV and the maximum observed $t\bar{t}$ invariant mass is 4.1 TeV.

The distributions of second-leading jet p_{T} as a function of the leading top-quark-jet p_{T} are shown in Figure 5. The distributions of the top-quark-jet p_{T} fall more rapidly than the predictions.

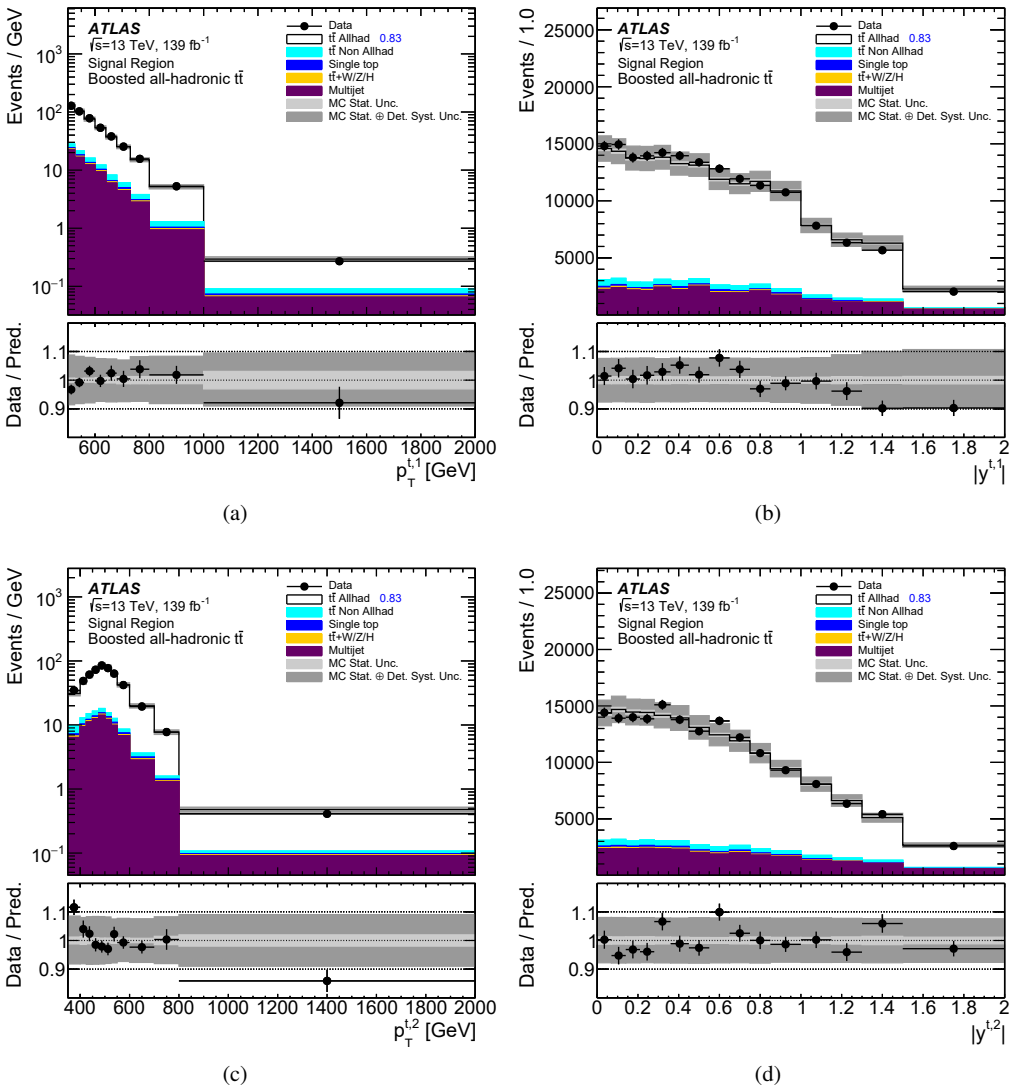

Figure 4: Kinematic distributions of top-quark-candidate jets in the signal region: (a) p_{T} and (b) $|y|$ of the leading jet, and (c) p_{T} and (d) $|y|$ of the second-leading jet. The signal prediction (open histogram) is based on the Powheg+Pythia 8 $t\bar{t}$ calculation normalized to the observed yield. The background (solid histogram) is the sum of the data-driven multijet estimate and the MC-based expectation for the contributions of non-all-hadronic $t\bar{t}$, single-top-quark, and $t\bar{t}+W/Z/H$ processes. The light grey bands indicate the statistical uncertainties and the dark grey bands indicate the combined statistical and detector-related systematic uncertainties defined in Section 8.

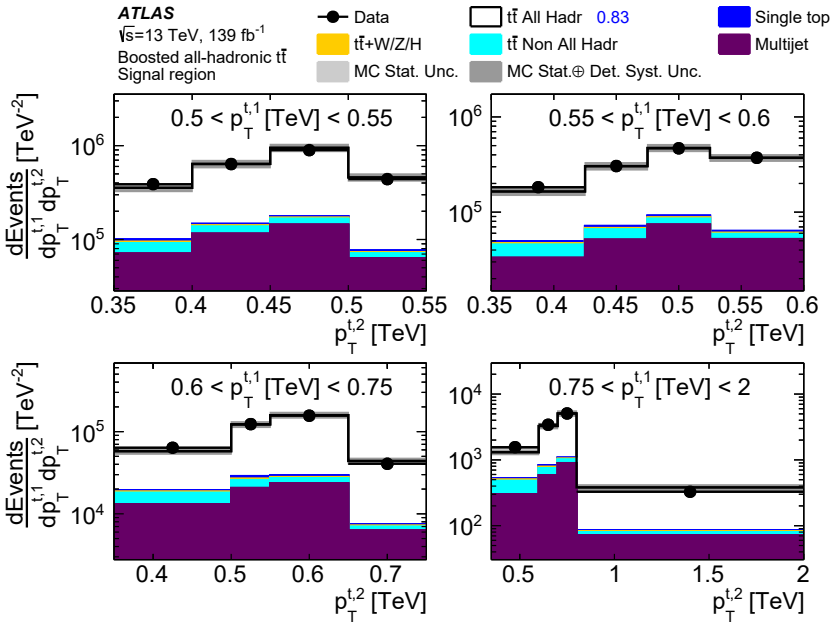

(a)

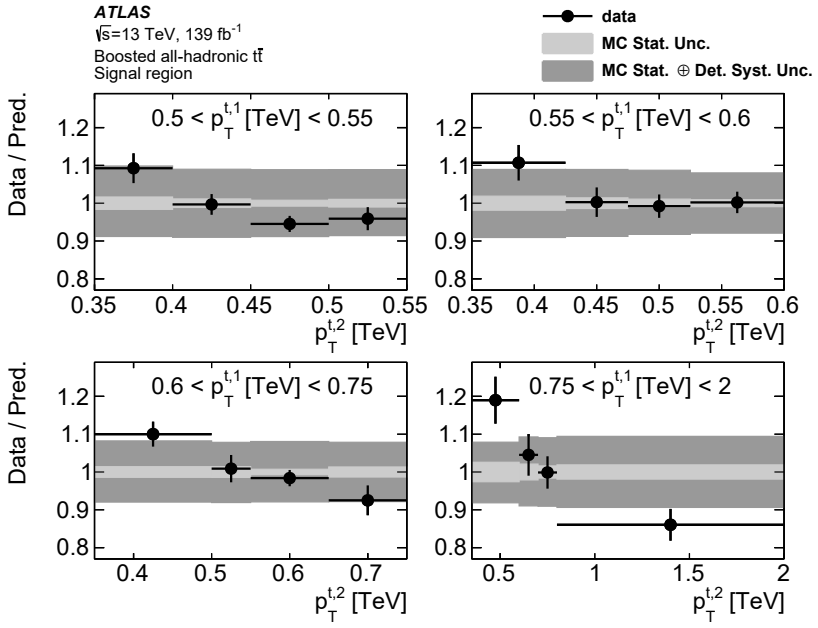

(b)

Figure 5: Two-dimensional kinematic distributions of second-leading jet p_{T} versus leading-jet p_{T} in the signal region: (a) the differential event yield as a function of the p_{T} of the leading jet and p_{T} of second-leading jet, and (b) the ratio of the observed and predicted distributions. The signal prediction (open histogram) is based on the POWHEG+PYTHIA 8 $t\bar{t}$ calculation normalized to the observed yield. The background (solid histogram) is the sum of the data-driven multijet estimate and the MC-based expectation for the contributions of non-all-hadronic $t\bar{t}$, single-top-quark, and $t\bar{t}+W/Z/H$ processes. The light grey bands indicate the statistical uncertainties and the dark grey bands indicate the combined statistical and detector-related systematic uncertainties defined in Section 8.

7 Correction procedures

The observed differential cross-sections reflect the underlying physics processes as well as the acceptance, efficiency, and resolution of the detector and reconstruction algorithms. These distributions are unfolded to particle level in a fiducial phase space in order to correct for detector effects. The correction is made to the particle-level differential cross-sections, i.e. the distributions defined by the stable particles in the MC simulation.

Parton-level differential cross-sections are measured in a similar manner. The parton level is defined in the MC simulation by the top quark after final-state radiation, i.e. immediately before its decay.

The following subsections describe the particle-level fiducial phase space, the parton-level fiducial phase space, and the algorithm used for the unfolding.

7.1 Particle-level fiducial phase-space and parton-level fiducial phase-space regions

The particle-level fiducial phase-space definition is intended to match the kinematic requirements used to select the $t\bar{t}$ process as described in Section 4.2. Particle-level jets and leptons are defined so as to closely match the detector-level objects.

In the MC signal sample, electrons and muons that do not originate from hadron decays are 'dressed' with prompt photons found in a cone of size $\Delta R = 0.1$ around the lepton direction. The four-momentum of each photon in the cone is added to the four-momentum of the lepton to produce the dressed lepton. The leptons within $\Delta R = 0.4$ of a small-R jet, as defined below, are removed.

Jets are clustered using all stable particles (lifetimes > 30 ps) except those used in the definition of dressed electrons, dressed muons, and neutrinos not from hadron decays, using the anti-k_t algorithm with a radius parameter $R = 1.0$ for large-R jets and $R = 0.4$ for small-R jets [115]. The decay products of hadronically decaying τ-leptons are included. These jets include the particles from the underlying event in the pp collision but do not include particles from additional interactions in the same pp bunch crossing. Large-R jets are required to have $p_{\mathrm{T}} > 350$ GeV and a mass within 50 GeV of the top-quark mass. Small-R jets are required to have $p_{\mathrm{T}} > 25$ GeV and $|\eta| < 2.5$.

The requirements on particle-level objects in the all-hadronic $t\bar{t}$ MC events define the particle-level fiducial phase space: (1) there can be no dressed electrons or muons with $p_{\mathrm{T}} > 25$ GeV and $|\eta| < 2.5$ in the event, (2) there must be at least two anti-k_t $R = 1.0$ jets with $p_{\mathrm{T}} > 350$ GeV, $|\eta| < 2.0$, and jet mass between 122.5 and 222.5 GeV, (3) there must be at least one anti-k_t $R = 1.0$ jet with $p_{\mathrm{T}} > 500$ GeV and $|\eta| < 2.0$, and (4) each of the two leading $R = 1.0$ jets must be matched to a b-hadron with $p_{\mathrm{T}} > 5$ GeV using a ghost-matching technique [109]. The use of η instead of rapidity for defining the fiducial phase space was motivated by its use in the event selection at detector level. These requirements are used to derive the migration matrices, efficiency corrections, and acceptance corrections needed for the unfolding procedure.

The parton-level fiducial phase space is defined by requiring that the leading top quark have $p_{\mathrm{T}} > 500$ GeV and the second-leading top quark have $p_{\mathrm{T}} > 350$ GeV. No rapidity or other kinematic requirements are applied.

7.2 Unfolding algorithm

The iterative Bayesian method [116] as implemented in RooUnfold [117] is used to correct the detector-level event distributions to their corresponding particle- and parton-level differential cross-sections. The unfolding starts from the observed differential distributions after subtraction of the estimated backgrounds.

The unfolding step for each observable uses a migration matrix ($\mathcal{M}$) derived from simulated $t\bar{t}$ events by binning the events in the particle-level (parton-level) fiducial phase space using the true value for the observable and subdividing the events in each particle-level (parton-level) bin into bins of the detector-level observable. The resulting matrix, defined by the detector-level observable bins on the x-axis and the particle-level (parton-level) bins on the y-axis, is normalized so that each row sums to unity, as shown in Figure 6.

The bin widths are chosen by considering the measurement resolution of a given observable to achieve the migration matrix to be largely diagonal and that the unfolding procedure is stable, as determined by the stress tests described below. The migration matrices for the rapidity of the leading and second-leading top-quark candidates are the exceptions, where there are a small number of entries in very off-diagonal bins. This is due to cases where the two large-R jets swap order in p_{T} when they evolve from the particle level or parton level to the detector level.

The efficiency corrections $\epsilon^{i}_{\mathrm{eff}}$ correct for events that are in the particle-level (parton-level) fiducial phase space but are not reconstructed at detector level. The acceptance corrections f^{j}_{acc} account for events that are generated outside the particle-level (parton-level) fiducial phase space but pass the detector-level selection. Figure 7 shows the efficiency and acceptance corrections for the p_{T} and rapidity of the leading jet. The variations in acceptance as a function of rapidity arise from transitions from one calorimeter system to another. The corrections for the other observables show similar behaviour except for observables sensitive to the relative orientation of the two top-quark jets: $p_{\mathrm{T}}^{t\bar{t}}$, $\left|\Delta\phi^{t\bar{t}}\right|$, and $\left|p_{\mathrm{out}}^{t\bar{t}}\right|$, which show modest decreases in acceptance.

The unfolding procedure for an observable X at both particle- and parton-level is summarized by the heuristic expression

$$\frac{\mathrm{d}\sigma^{\mathrm{fid}}}{\mathrm{d}X^{i}} \equiv \frac{1}{\int \mathcal{L}\,\mathrm{d}t \cdot \Delta X^{i}} \cdot \frac{1}{\epsilon^{i}_{\mathrm{eff}}} \cdot \sum_{j} \mathcal{M}^{-1}_{ij} \cdot f^{j}_{\mathrm{acc}} \cdot \left(N^{j}_{\mathrm{reco}} - N^{j}_{\mathrm{bg}}\right), \tag{2}$$

where N^{j}_{reco} and N^{j}_{bg} refer to the number of reconstructed signal and background events in each detector-level bin, respectively; the index j runs over bins of X at detector level while the index i labels bins at particle level; ΔX^{i} is the bin width; and $\int \mathcal{L}\,\mathrm{d}t$ is the integrated luminosity. The matrix $\mathcal{M}^{-1}_{ij}$ denotes the unfolding procedure and, strictly speaking, is not the inverse of the migration matrix defined earlier but is determined iteratively and has the effect of inverting the smearing resulting from the measurement process.

This unfolding procedure, expressed in Eq. (2), is performed iteratively and regularizes the smoothness of the unfolded distribution. Studies of the performance of the algorithm using MC events show that four iterations provide stable unfolded distributions with high precision.

The inclusive cross-section, σ^{fid}, for $t\bar{t}$ events in the particle-level (parton-level) phase space, obtained by integrating the differential cross-section, is used to determine the normalized differential cross-section $1/\sigma^{\mathrm{fid}} \cdot \mathrm{d}\sigma^{\mathrm{fid}}/\mathrm{d}X^{i}$. The particle-level fiducial phase-space cross-section is not corrected for the all-hadronic $t\bar{t}$ branching fraction of 0.457 [118]. This branching fraction is used to correct the parton-level fiducial

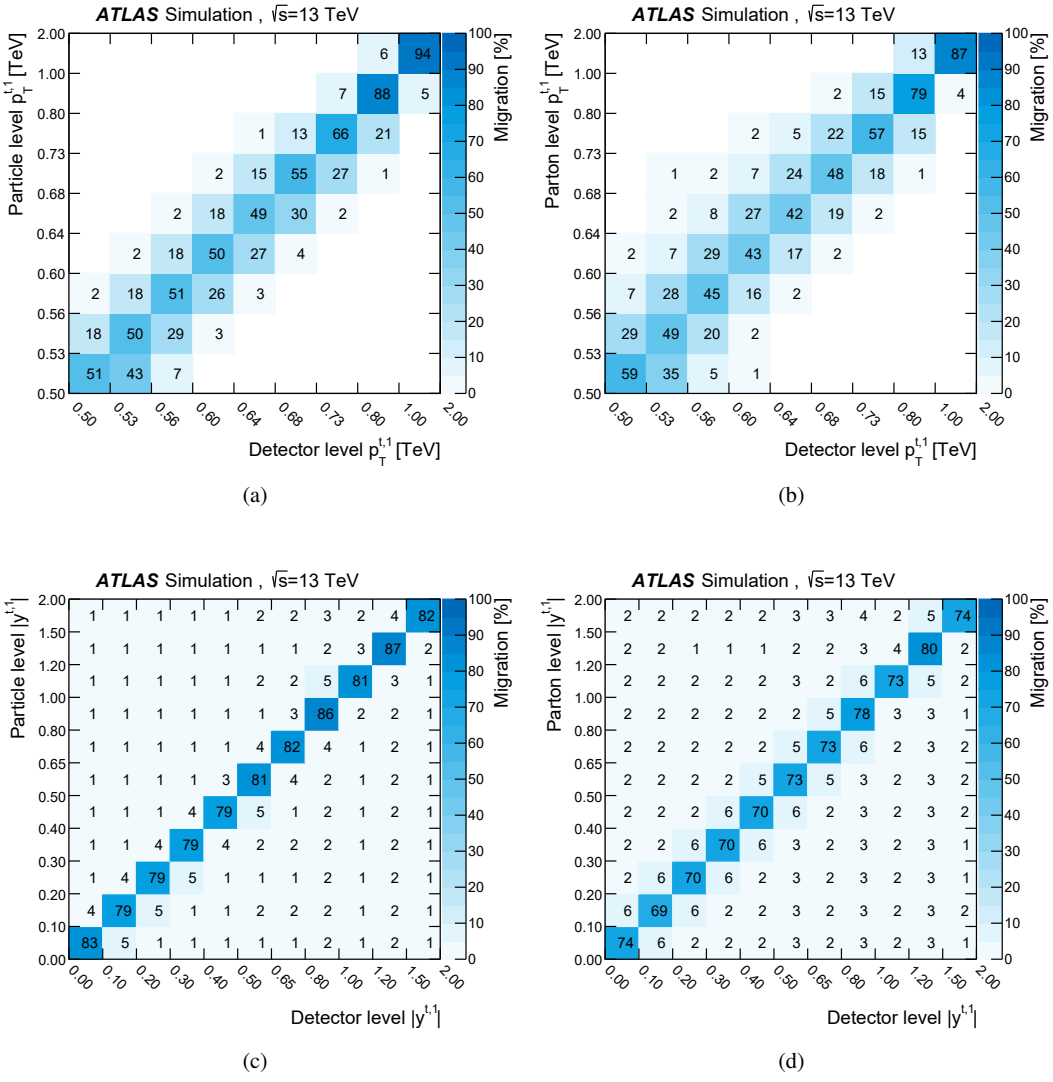

Figure 6: Migration matrices for p_{T} and $|y|$ of the leading top-quark jet for the particle-level fiducial phase space in (a) and (c), respectively, and for the parton-level fiducial phase space in (b) and (d), respectively. Each row is normalized to 100%. The POWHEG+PYTHIA 8 generator together with the GEANT4 detector simulation framework is used to determine these matrices.

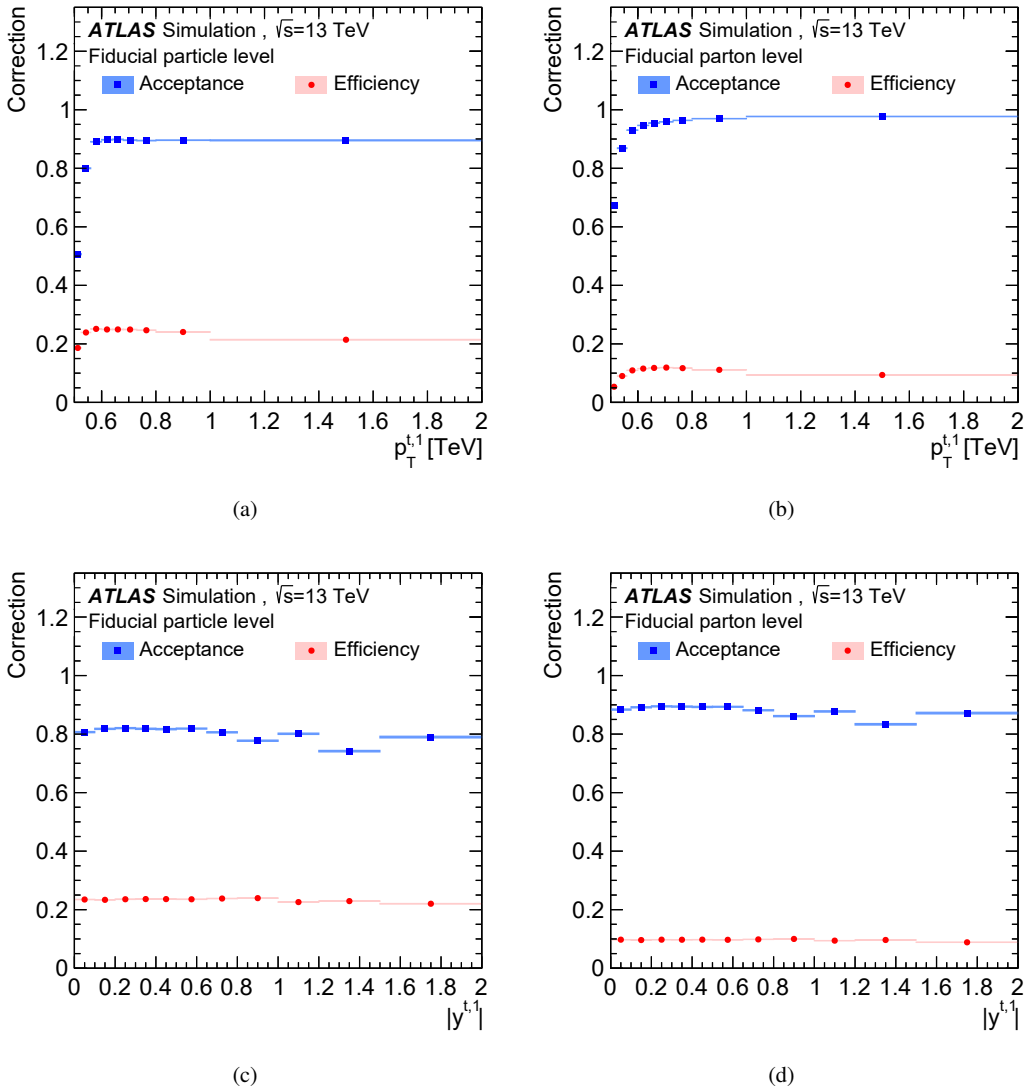

Figure 7: Acceptance and efficiency corrections as a function of the leading top-quark-jet p_{T} and $|y|$ for the particle-level phase space are shown in (a) and (c), respectively, and for the parton-level fiducial phase space in (b) and (d), respectively. The observables on x-axes are at the truth level when used for the efficiency correction while they are at the detector level when used for the acceptance correction. The POWHEG+PYTHIA 8 generator together with the GEANT4 detector simulation framework is used to correct for detector effects. The blue and red bars represent statistical uncertainties.

phase-space cross-section measurement in order to facilitate a comparison with NNLO fixed-order predictions.

Tests are performed at both particle level and parton level to verify that the unfolding procedure recovers the generator-level distributions for input distributions that vary from the observed distributions or nominal predictions by factors consistent with the statistical uncertainties in the observed distributions. These stress tests show that the results of the unfolding procedure are unbiased as long as the variations in the input distributions are consistent with the measurement resolution of the observable.

8 Systematic and statistical uncertainties

Systematic uncertainties introduced by the particle and jet reconstruction and calibration, the $t\bar{t}$ modelling, and the background estimation are described below. The propagation of systematic uncertainties through the unfolding procedure is described in Section 8.2. The treatment of the statistical uncertainties associated with the MC calculations is also discussed.

8.1 Estimation of systematic uncertainties

The systematic uncertainties of the measured distributions are estimated using simulation samples and the data satisfying the final selection requirements.

A significant source of systematic uncertainty is the jet-energy scale (JES) for the large-R jets [110]. The small-R jet JES [111] does not contribute to the systematic uncertainties as these jets are not used in the event selection nor the unfolding procedures. Uncertainties in the jet energy resolution (JER) for large-R jets is also considered [110, 111]. The effect of correlations between the JES and JER systematic uncertainties is negligible in this analysis. The JES uncertainty results in a cross-section uncertainty that is typically of 4%–5% but reaches 12% for rapidity-related observables at large rapidity values. The JER uncertainty creates a cross-section uncertainty of 2%–5%.

The uncertainties in the large-R jet mass scale (JMS) and resolution (JMR) are derived from observations of the W boson and top-quark masses in semileptonic $t\bar{t}$ events [110, 119], and by measuring the double ratio of data to MC simulation for calorimeter-only and track-only quantities. The effect of the JMS uncertainty is typically around 1%–2%, while the effect of the JMR uncertainty is below 1%.

The efficiency to top-quark-tag large-R jets is corrected in simulated events by applying top-quark-tagging scale factors to account for a residual difference between data and simulation samples [28, 29]. The signal jets are required to be top-quark-tagged while other jets are labelled as background jets. Uncertainties in the rate of background jets were measured in two phase-space regions enriched in multijet and γ + jet processes. The signal-jet uncertainties were measured in boosted $t\bar{t}$ lepton+jets events. Additional uncertainties are assigned to cover signal-modelling effects and extrapolation beyond the fiducial phase-space regions. The associated systematic uncertainties are computed by varying the top-quark-tagging scale factors within their uncertainties and are found to create differential cross-section uncertainties ranging from 7% to 10%.

The efficiency to tag variable-R jets containing b-hadrons is corrected in simulated events by applying b-tagging scale factors, extracted from $t\bar{t}$ events, in order to account for residual tagging-efficiency differences between data and simulation [30, 31]. An additional uncertainty is included for the extrapolation of the measured uncertainties to the high-p_{T} region of interest [120]. Its estimation is improved for the

jets passing the event selection of this measurement by using the b-hadron p_{T} spectrum corresponding to these jets. The systematic uncertainty is computed by varying the b-tagging scale factors within their uncertainties and is found to be 3%.

The cross-section uncertainties arising from the lepton energy scale, resolution, and identification efficiency are below 0.1% [100, 101].

For backgrounds estimated by MC simulation, the uncertainties in the predicted production cross-sections are included. An additional uncertainty of 50% is assigned to the Wt single-top-quark production cross-section to cover the large difference between the rates predicted by the diagram-removal [77] and diagram-subtraction [77] schemes in the boosted regime [121]. These schemes have different treatments of the overlap of the Wt-channel with $t\bar{t}$ production. Systematic uncertainties affecting the multijet-background estimate come from the subtraction of other background processes in the control regions and from the uncertainties in the measured tagging correlations. The detector-related uncertainties which affect the MC-based background processes in the control regions used for the multijet-background estimates are directly accounted for in the above-mentioned detector systematic uncertainty categories. The remaining multijet-background uncertainties range from 1% to 6% for leading large-R jets with p_{T} from 500 GeV to 2 TeV, respectively.

Alternative MC generators are employed to assess modelling systematic uncertainties. In these cases, the difference between the unfolded distribution from an alternative model and its own particle-level or parton-level distribution is used as the estimate of the corresponding systematic uncertainty in the unfolded differential cross-section. The matrices from the nominal MC simulation are used in the unfolding.

To assess the uncertainty related to the matrix-element calculation and the parton-shower matching procedure, aMC@NLO+Pythia 8 events are unfolded using the migration matrix and correction factors derived from the Powheg+Pythia 8 sample with the matrix-element correction turned off. This uncertainty is typically a few percent, increasing to 5%–10% at large $p_{\mathrm{T}}^{t\bar{t}}$ and $|p_{\mathrm{out}}^{t\bar{t}}|$, and small $\Delta\phi^{t\bar{t}}$. To assess the uncertainty associated with the choice of parton-shower and hadronization model, a comparison is made between the unfolded and generator-level distributions of simulated events created with the Powheg+Herwig 7 generator but using the nominal corrections and migration matrices. The resulting systematic uncertainties, taken as the symmetrized difference, are found to be less than 5%.

The uncertainty related to the modelling of initial- and final-state radiation is determined by using $t\bar{t}$ MC samples with modified ISR/FSR settings [122]. Four different upward/downward variations of MC simulation parameters are performed to assess the ISR uncertainty; these have a significant effect on initial-state radiation, while the effect on final-state radiation is small. The upward (downward) variations are defined by scaling of each of μ_{r} and μ_{f} by a factor of 0.5 (2), the setting of h_{damp} to $3m_{\mathrm{top}}$ ($1.5m_{\mathrm{top}}$), and the variation of the A14 tuned set of parameters encoded by the Var3cUp (Var3cDown) parameter [66, 122]. The effects caused by independent variations of individual parameters are summed in quadrature to define the ISR uncertainty. For FSR, variations are defined by scaling μ_{r} and μ_{f} for FSR only. The FSR-up variation uses a scale factor of 0.5 while the FSR-down variation uses a factor of 2. This uncertainty is found to be approximately 5% or lower depending on the observable considered.

The uncertainty arising from PDFs is assessed using the Powheg+Pythia 8 $t\bar{t}$ sample. The uncertainty in the unfolded distributions arising from the uncertainties in the PDF4LHC15 PDF set is determined using the Hessian approach [87]. This uncertainty is found to be approximately 1%.

The effect of varying the top-quark mass by ±1 GeV had a negligible effect on the unfolded results.

The uncertainty in the combined Run 2 integrated luminosity is 1.7% [123], obtained using the LUCID-2 detector [124] for the primary luminosity measurements. This uncertainty affects the rate of backgrounds estimated using MC calculations. It also affects the overall normalization as seen in Eq. (2), but has negligible effect on the normalized differential cross-section measurements. The uncertainty arising from the size of the nominal MC sample is approximately 1%.

8.2 Propagation of systematic uncertainties and treatment of correlations

The statistical and systematic uncertainties are propagated and combined in the same way for both the particle-level and parton-level results, using pseudo-experiments created from the nominal and alternative MC samples.

To evaluate the impact of a systematic-uncertainty contribution to an unfolded distribution, a corresponding distribution is obtained from simulations employing modified parameter settings reflecting this particular contribution. This distribution is then unfolded using corrections obtained with the nominal Powheg+Pythia 8 sample. The resulting unfolded distribution is compared with the corresponding particle- or parton-level distribution and the difference is taken as the uncertainty in the unfolded measurement. For each systematic uncertainty, the correlation between the uncertainties in the signal and background distributions is taken into account. All detector- and background-related systematic uncertainties are estimated using the nominal Powheg+Pythia 8 sample. Residual hard-scattering, parton-shower and hadronization, ISR/FSR, and PDF uncertainties are estimated from a comparison between the unfolded cross-section and the corresponding particle- or parton-level distribution produced using the corresponding MC generator. This method is used to estimate the systematic uncertainties due to the choice of MC generator.

The systematic uncertainties for the particle-level fiducial phase-space cross-section measurement described in Section 9 are listed in Table 3. Figure 8 shows a summary of the relative size of the systematic uncertainties for the leading top-quark-jet p_{T} and rapidity distributions at particle level and parton level. For the second-leading jet, the uncertainty is ~8% at $p_{\mathrm{T}} = 350$ GeV and ~14% for $p_{\mathrm{T}} > 800$ GeV at particle level.

The effect of the statistical uncertainty of the data, the statistical uncertainty due to the size of MC samples, and the systematic uncertainties are incorporated into pseudo-experiments to determine the covariance matrix of the measurement, following the approach used in Refs. [10, 14]. The effect of the statistical uncertainty of the data is incorporated by independent Poisson fluctuations in each data bin. The statistical uncertainty due to the size of the background MC samples is incorporated by adding independent Gaussian fluctuations in each bin of the signal region and control regions used for the multijet-background estimation. The statistical uncertainty due to the size of the signal MC samples is incorporated by adding Gaussian fluctuations in the unfolding corrections and migration matrices, and in each bin of the distributions in the control regions used in the multijet-background estimation. The effects of all other systematic uncertainties are incorporated into the pseudo-experiments by including Gaussian fluctuations associated with each source of uncertainty. A covariance matrix is constructed using these pseudo-experiments for each differential cross-section in order to include the effect of all uncertainties and correlations on the bin-to-bin measurements to allow quantitative comparisons with theoretical calculations.

The comparison between the measured differential cross-sections and a variety of MC calculations is quantified by calculating χ^2 values employing the covariance matrix and by calculating the corresponding

Source	Relative Uncertainty [%]
Top-tagging	7.8
JES ⊕ JER	4.2
JMS ⊕ JMR	1.1
Flavour tagging	2.9
Alternative hard-scattering model	0.9
Alternative parton-shower model	4.3
ISR/FSR + scale	4.9
PDF	0.8
Luminosity	1.7
MC sample statistics	0.4
Total systematic uncertainty	11.8
Statistical uncertainty	1.0
Total uncertainty	11.8

Table 3: Summary of the largest systematic and statistical relative uncertainties for the total particle-level fiducial phase-space cross-section measurement. The uncertainties that are significantly less than 1% are not listed.

p-values from the χ^2 and the number of degrees of freedom (NDF). The χ^2 values are obtained using

$$\chi^2_{N_\mathrm{b}} = V^\mathrm{T}_{N_\mathrm{b}} \cdot \mathrm{C}^{-1}_{N_\mathrm{b}} \cdot V_{N_\mathrm{b}} \,,$$

where V_{N_b} is the vector of differences between the measured differential cross-section values and calculations, $\mathrm{C}^{-1}_{N_\mathrm{b}}$ is the inverse of the covariance matrix, and N_b is the number of bins in the unfolded distribution.

The normalization constraint used to derive the normalized differential cross-sections lowers the NDF to one less than the rank of the $N_\mathrm{b} \times N_\mathrm{b}$ covariance matrix. The χ^2 for the normalized differential cross-sections is

$$\chi^2_{N_\mathrm{b}-1} = \hat{V}^\mathrm{T}_{N_\mathrm{b}-1} \cdot \hat{\mathrm{C}}^{-1}_{N_\mathrm{b}-1} \cdot \hat{V}_{N_\mathrm{b}-1} \,,$$

where $\hat{V}_{N_\mathrm{b}-1}$ is the vector of differences between measured normalized differential cross-section values and calculations obtained by discarding one of the N_b elements, and $\hat{\mathrm{C}}_{N_\mathrm{b}-1}$ is the $(N_\mathrm{b}-1) \times (N_\mathrm{b}-1)$ sub-matrix derived from the covariance matrix corresponding to normalized differential cross-section measurement by discarding the corresponding row and column. The χ^2 does not depend on the index of the discarded row and column.

9 Measured differential cross-sections

All measurements are presented as single-differential, double-differential or triple-differential cross-sections in the particle-level and parton-level fiducial phase spaces. The total cross-section measurements in these fiducial phase spaces also provide a test of the total cross-section calculations for different models. Normalized differential cross-sections allow a comparison of their shapes between data and MC predictions while removing the effects of possible differences in the yields.

The particle-level and parton-level fiducial phase-space cross-sections and the normalized fiducial phase-space differential cross-sections are presented below.

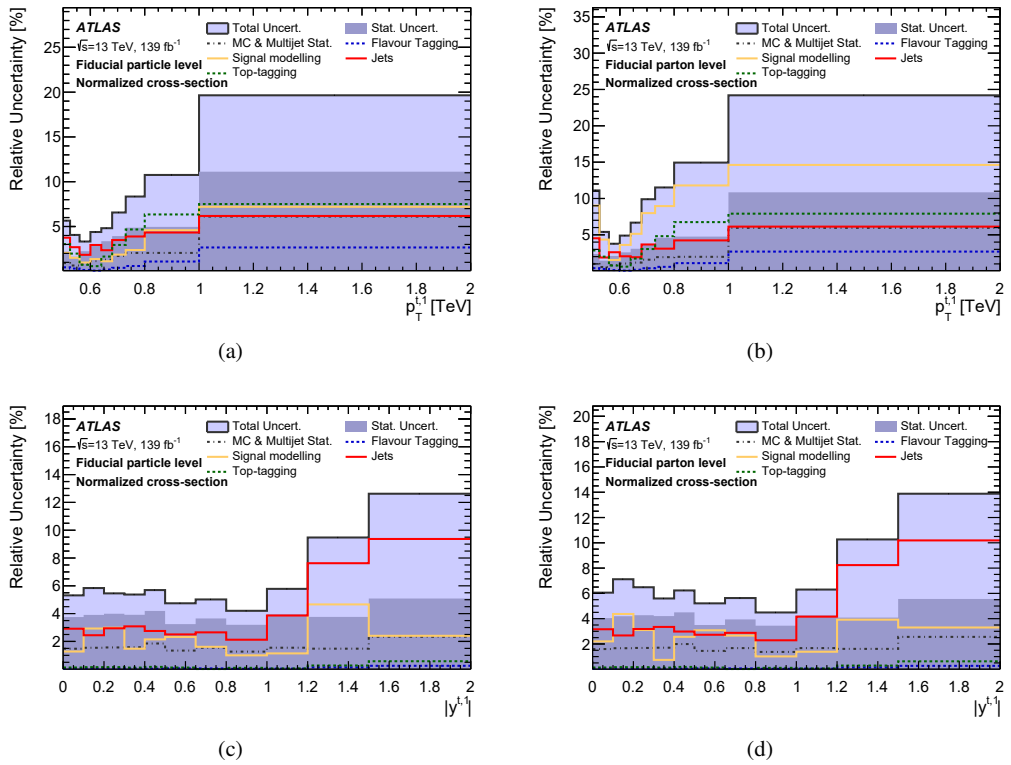

Figure 8: Relative uncertainties in the normalized differential cross-sections as a function of the leading top-quark-jet p_T and rapidity at particle level ((a) and (c)) and parton level ((b) and (d)). The light and dark blue areas represent the total and statistical uncertainty, respectively. The POWHEG+PYTHIA 8 generator is used as the nominal prediction to correct for detector effects.

These measurements are compared with SM predictions using the nominal POWHEG+PYTHIA 8 MC samples, the POWHEG+HERWIG 7 alternative parton-showering and hadronization calculations, the AMC@NLO +PYTHIA 8 alternative matrix-element calculation, and the POWHEG+PYTHIA 8 samples using modified ISR and FSR settings. The sample with less ISR and FSR ('less IFSR') has the factorization and renormalization scales increased by a factor of two compared to the nominal sample, and the A14 Var3c Down tune variation in the parton shower. The sample with more ISR and FSR ('more IFSR') has $h_{\text{damp}} = 3m_{\text{top}}$, the factorization and renormalization scales reduced by a factor of 0.5 compared to the nominal sample, and the A14 Var3c Up tune variation in the parton shower.

9.1 Total particle-level cross-section in the fiducial phase space

The particle-level fiducial phase-space cross-section, multiplied by the $t\bar{t}$ all-hadronic decay branching fraction, is used to normalize the observed particle-level fiducial phase-space differential cross-sections. It is determined by taking the observed yield after background subtraction and applying the correction factors to account for events that were produced outside the fiducial phase-space region but passed the detector-level selection criteria, and the event-selection efficiency. This procedure amounts to a single-bin

unfolding. All of the systematic uncertainties that affect the correction and acceptance are included in this measurement.

The particle-level fiducial phase-space cross-section is

$$\sigma^{t\bar{t},\text{fid}}_{\text{particle}} \times B(t\bar{t} \to \text{hadrons}) = 331 \pm 3(\text{stat.}) \pm 39(\text{syst.})\ \text{fb}.$$

The measured fiducial phase-space cross-section times branching fraction can be compared with the cross-section predicted by the POWHEG+PYTHIA 8 particle-level calculation of 398^{+48}_{-49} fb, after normalizing its inclusive prediction to the NNLO+NNLL total $t\bar{t}$ cross-section. The associated uncertainty includes the statistical, scale, PDF, and NNLO+NNLL total inclusive calculation uncertainty. This measurement and the comparisons with predictions are shown in Figure 9.

9.2 Particle-level fiducial phase-space differential cross-sections

The normalized particle-level fiducial phase-space differential cross-sections for nine observables selected for comparison are presented in Figures 10–12. Figure 10 shows the differential cross-sections for the p_{T} of the leading and second-leading top-quark jets, and the invariant mass of the $t\bar{t}$ system. The differential cross-sections for the rapidity of the leading and second-leading top-quark jets, and the rapidity of the $t\bar{t}$ system are shown in Figure 11. Measured rapidity distributions have relatively large fluctuations between neighbouring bins. These reflect fluctuations observed at the detector level and are consistent with statistical uncertainties. The differential cross-sections for observables sensitive to extra radiation (the p_{T} of the $t\bar{t}$ system, the out-of-plane momentum, and the azimuthal separation of the top-quark jets) are shown in Figure 12. The remaining distributions are presented in Appendix A.

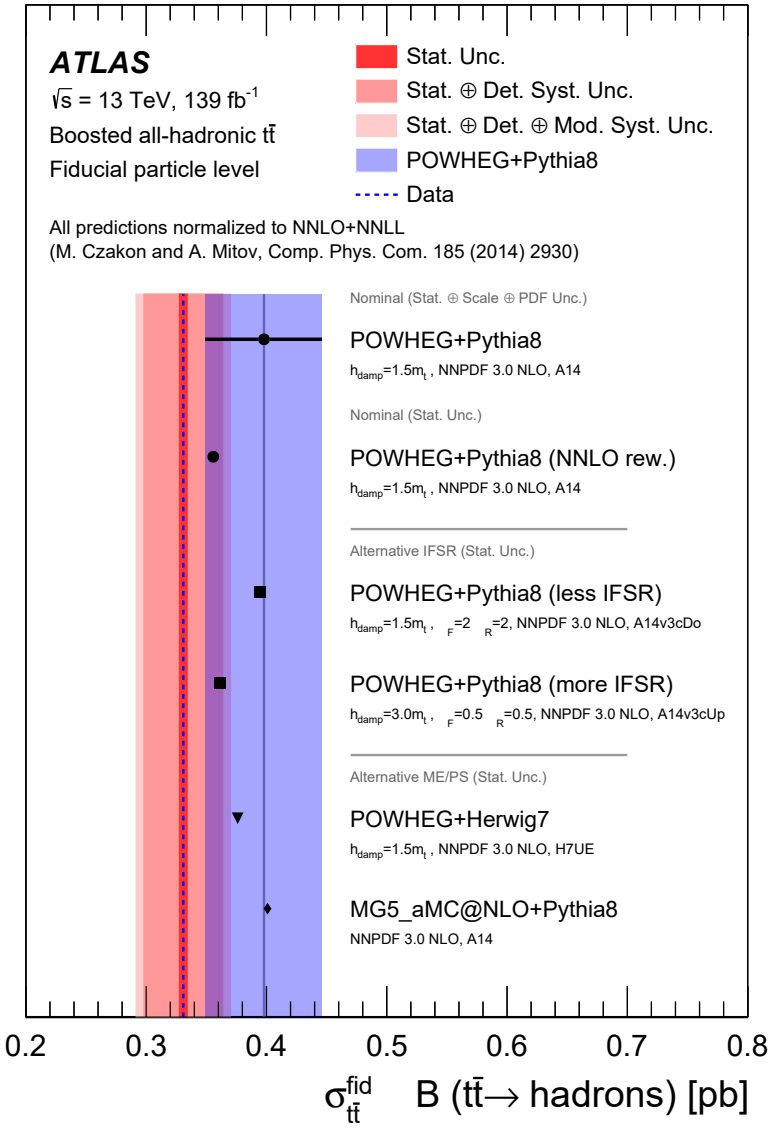

Figure 9: The particle-level cross-section in the fiducial phase space $\sigma_{t\bar{t}}^{\text{fid}}$ multiplied by the $t\bar{t}$ all-hadronic decay branching fraction $B(t\bar{t} \to \text{hadrons})$. The shaded (red) bands indicate the statistical, detector, and modelling uncertainties in the measurement. The POWHEG+PYTHIA 8 event generator is used as the nominal prediction to correct for detector effects. The uncertainty associated with the nominal POWHEG+PYTHIA 8 signal model (blue band) includes the statistical, scale, PDF, and NNLO+NNLL total inclusive calculation uncertainty. Other calculations show only the statistical uncertainty of the MC calculations, which is negligible and not visible in the figure. IFSR refers to both initial- and final-state radiation.

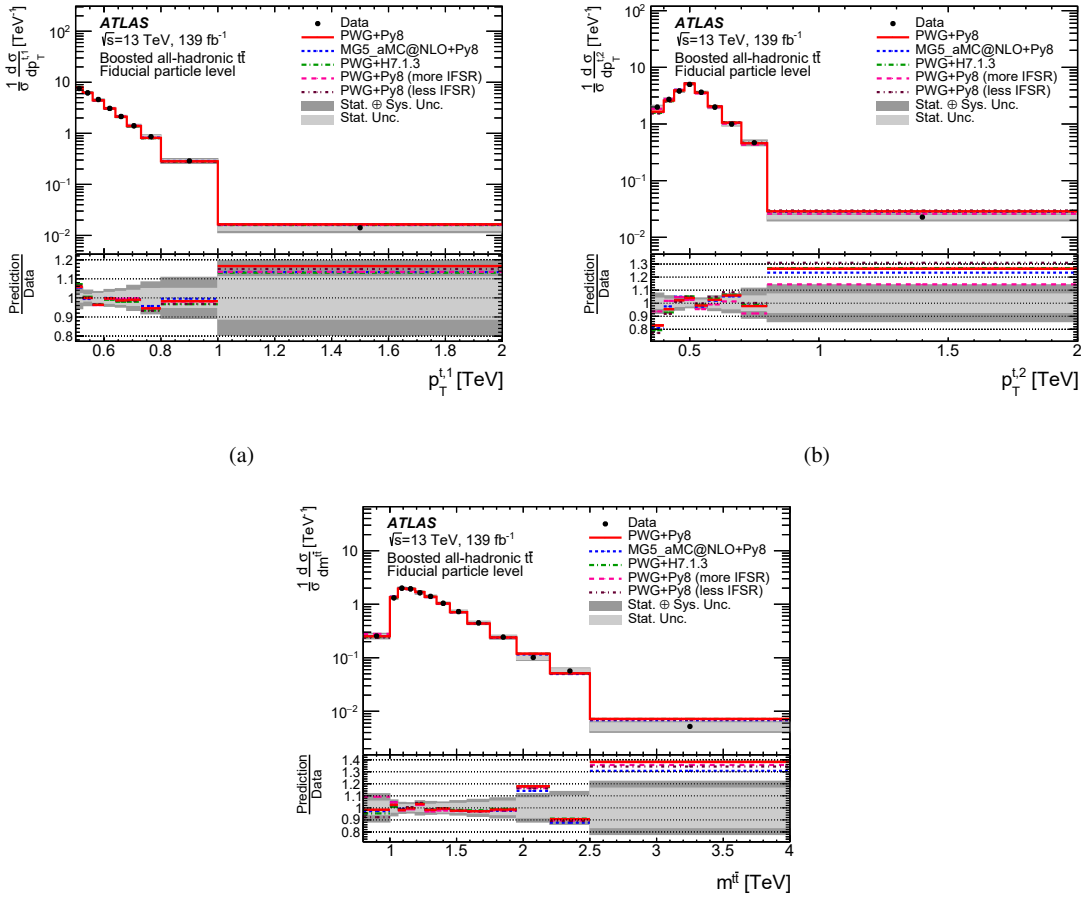

(a)

(b)

(c)

Figure 10: Normalized particle-level fiducial phase-space differential cross-sections as a function of (a) the p_{T} of the leading top-quark jet, (b) the p_{T} of the second-leading top-quark jet, and (c) the invariant mass of the $t\bar{t}$ system. The dark and light grey bands indicate the total uncertainty and the statistical uncertainty, respectively, of the data in each bin. Data points are placed at the centre of each bin. The POWHEG+PYTHIA 8 MC sample is used as the nominal prediction to correct the data to particle level.

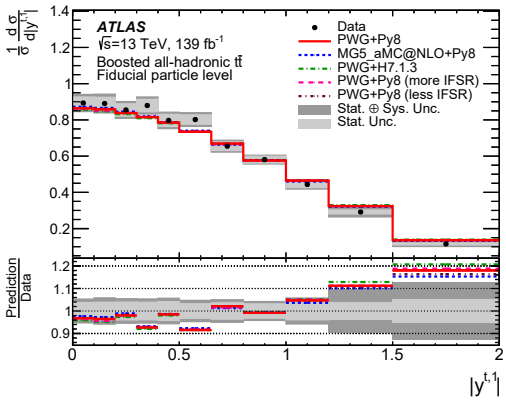

(a)

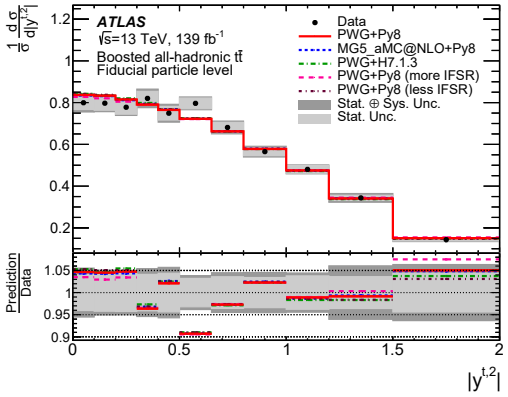

(b)

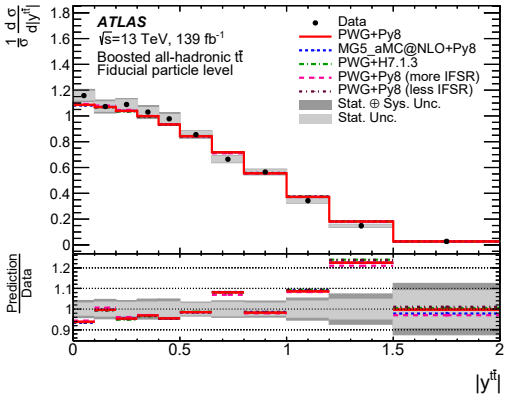

(c)

Figure 11: Normalized particle-level fiducial phase-space differential cross-sections as a function of the absolute value of the rapidity of (a) the leading top-quark jet, (b) the second-leading top-quark jet, and (c) the $t\bar{t}$ system. The dark and light grey bands indicate the total uncertainty and the statistical uncertainty, respectively, of the data in each bin. Data points are placed at the centre of each bin. The POWHEG+PYTHIA 8 MC sample is used as the nominal prediction to correct the data to particle level.

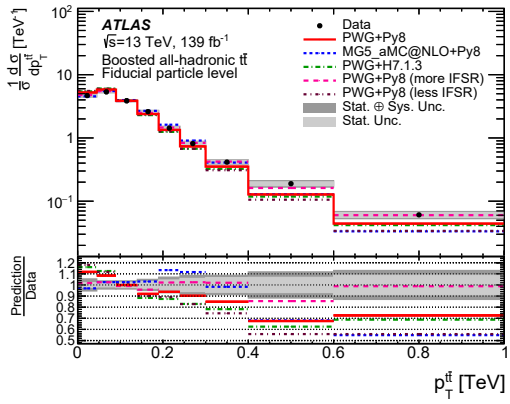

(a)

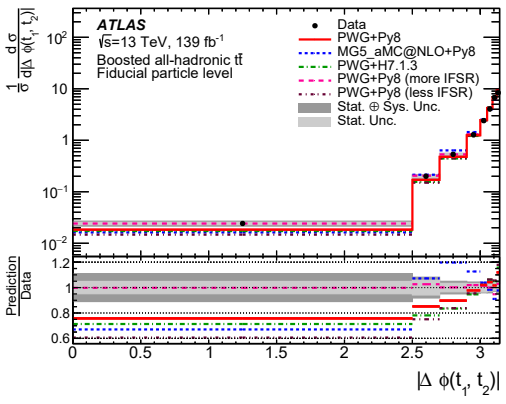

(b)

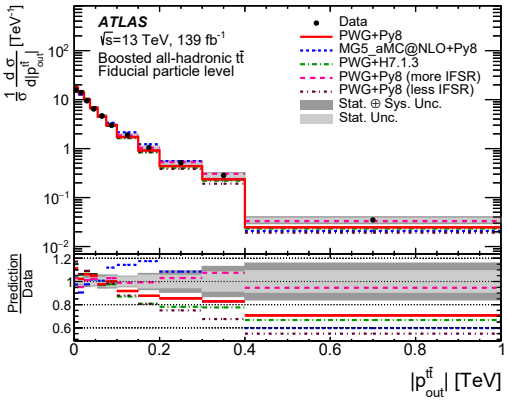

(c)

Figure 12: Normalized particle-level fiducial phase-space differential cross-sections as a function of (a) the p_{T} of the $t\bar{t}$ system, $p_{\mathrm{T}}^{t\bar{t}}$, (b) the azimuthal angle between the two top-quark jets, $\Delta\phi^{t\bar{t}}$, and (c) the absolute value of the out-of-plane momentum, $p_{\mathrm{out}}^{t\bar{t}}$. The dark and light grey bands indicate the total uncertainty and the statistical uncertainty, respectively, of the data in each bin. Data points are placed at the centre of each bin. The POWHEG+PYTHIA 8 MC sample is used as the nominal prediction to correct the data to particle level.

For a subset of the observables, pairs and triplets of variables are chosen to form double- and triple-differential cross-sections. These combinations of observables test specific aspects of the QCD predictions, where particular combinations have correlations that potentially differentiate between models. The selected set of fiducial phase-space double- and triple-differential cross-sections are shown in Figures 13–20. Additional double-differential cross-sections are presented in Appendix A.

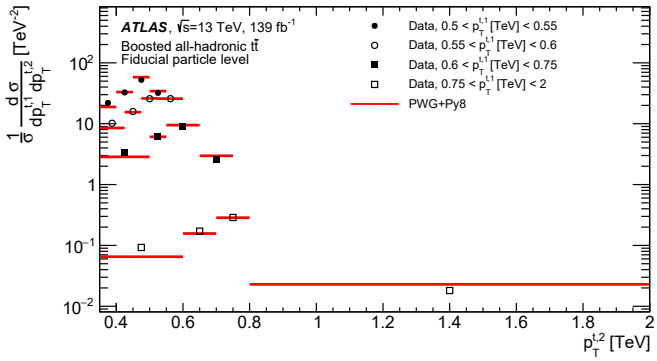

(a)

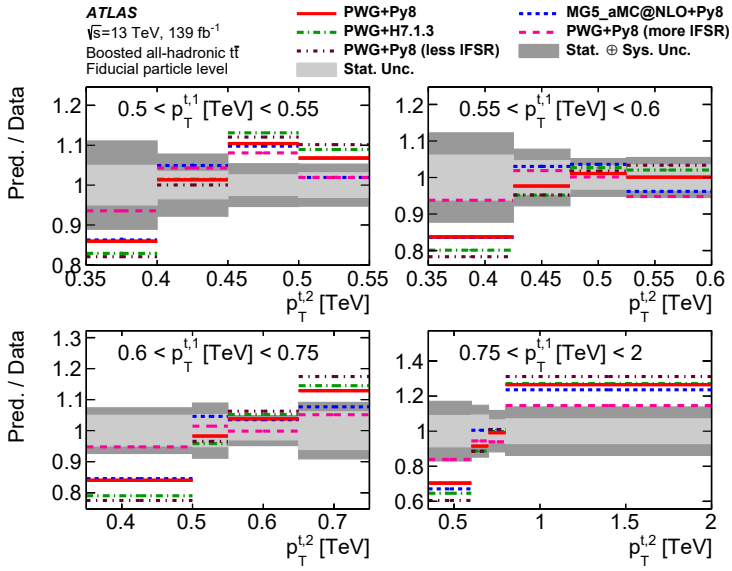

(b)

Figure 13: Normalized particle-level fiducial phase-space double-differential cross-sections as a function of the transverse momenta of the leading and second-leading top-quark jets, and comparisons with the POWHEG+PYTHIA 8 prediction are shown in (a). Data points are placed at the centre of each bin and the POWHEG+PYTHIA 8 predictions are indicated by solid lines. The ratios of various MC calculations to the normalized particle-level fiducial phase-space differential cross-sections are shown in (b). The dark and light grey bands indicate the total uncertainty and the statistical uncertainty, respectively, of the data in each bin.

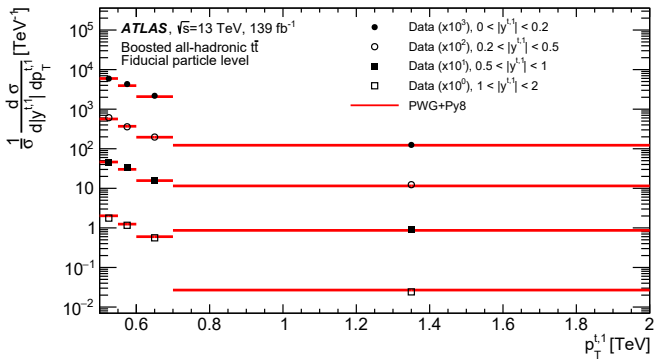

(a)

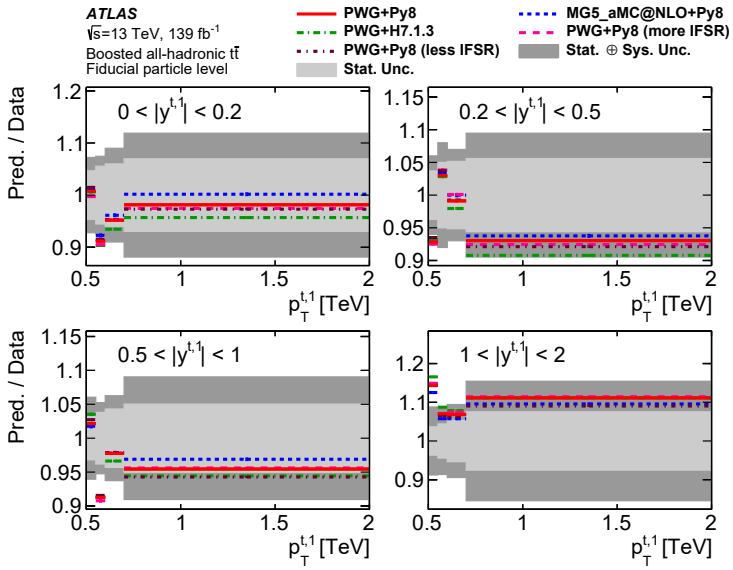

(b)

Figure 14: Normalized particle-level fiducial phase-space double-differential cross-sections as a function of the leading top-quark jet rapidity and p_{T}, and comparisons with the Powheg+Pythia 8 calculation are shown in (a). Data points are placed at the centre of each bin and the Powheg+Pythia 8 predictions are indicated by coloured lines. The measurement and the prediction are normalized by the factors shown in parentheses to aid visibility. The ratios of various MC predictions to the normalized fiducial phase-space differential cross-sections are shown in (b). The grey bands represent the statistical and total (statistical and systematic) uncertainties.

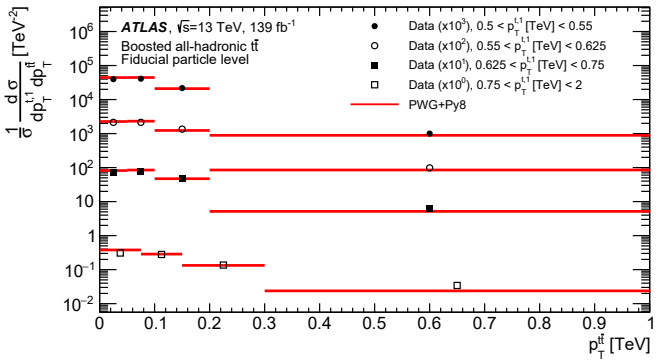

(a)

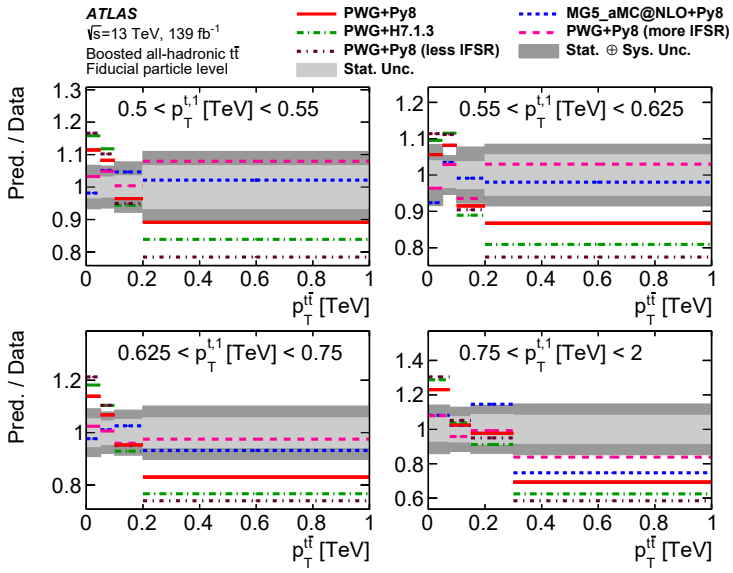

(b)

Figure 15: Normalized particle-level fiducial phase-space double-differential cross-sections as a function of the p_{T} of the leading top-quark jet and the p_{T} of the $t\bar{t}$ final state, $p_{\mathrm{T}}^{t\bar{t}}$, and comparisons with the Powheg+Pythia 8 calculation are shown in (a). Data points are placed at the centre of each bin and the Powheg+Pythia 8 predictions are indicated by solid lines. The measurement and the prediction are normalized by the factors shown in parentheses to aid visibility. The ratios of various MC calculations to the normalized fiducial phase-space differential cross-sections are shown in (b). The dark and light grey bands indicate the total uncertainty and the statistical uncertainty, respectively, of the data in each bin.

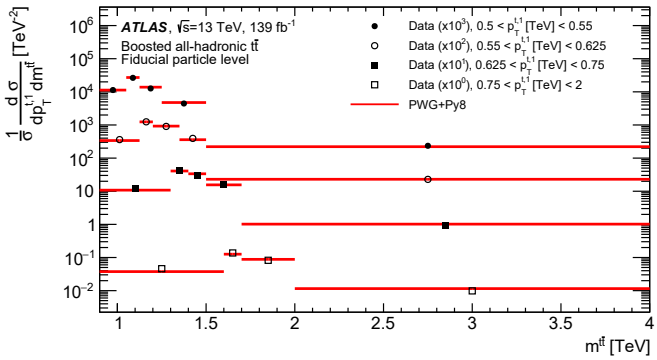

(a)

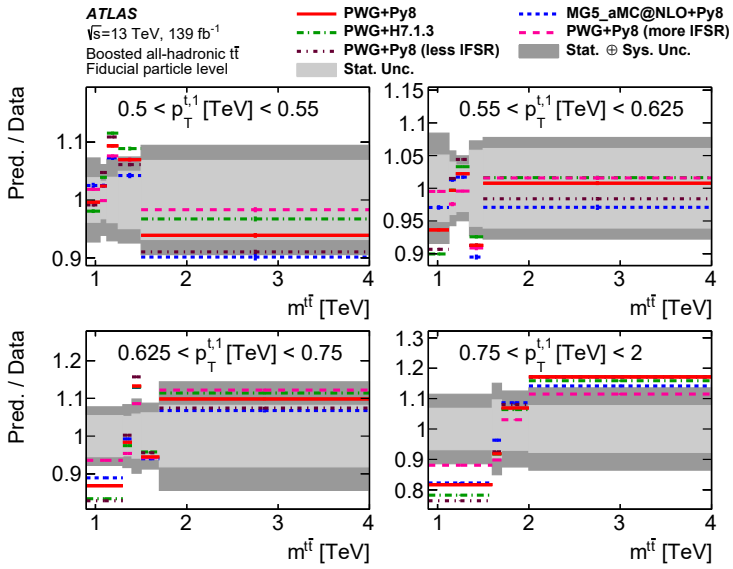

(b)

Figure 16: Normalized particle-level fiducial phase-space double-differential cross-sections as a function of the p_{T} of the leading top-quark jet and the invariant mass of the $t\bar{t}$ final state, $m^{t\bar{t}}$, and comparisons with the POWHEG+PYTHIA 8 predictions are shown in (a). Data points are placed at the centre of each bin and the POWHEG+PYTHIA 8 predictions are indicated by coloured lines. The measurement and the prediction are normalized by the factors shown in parentheses to aid visibility. The ratios of various MC predictions to the normalized fiducial phase-space differential cross-sections are shown in (b). The dark and light grey bands indicate the total uncertainty and the statistical uncertainty, respectively, of the data in each bin.

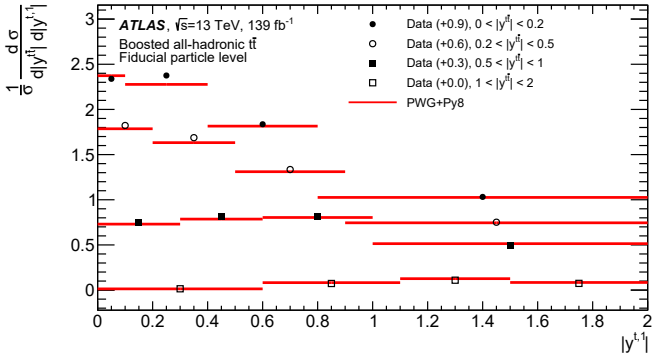

(a)

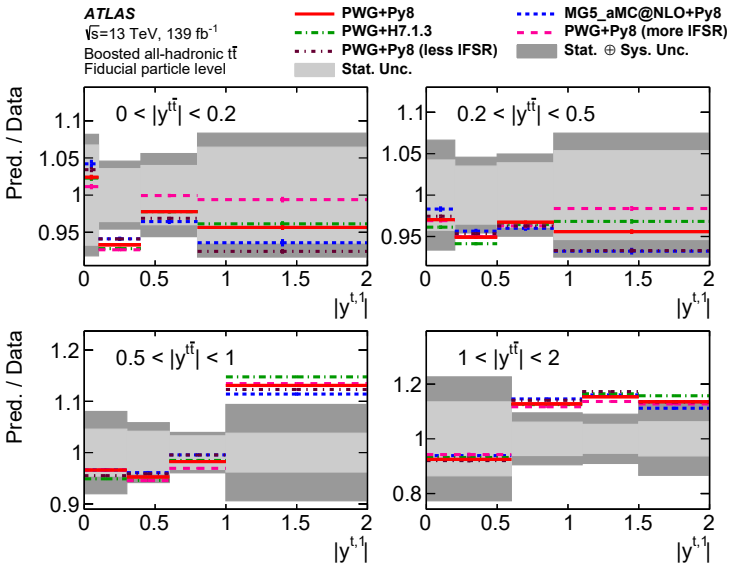

(b)

Figure 17: Normalized particle-level fiducial phase-space double-differential cross-sections as a function of the absolute value of the rapidity of the $t\bar{t}$ final state, $|y^{t\bar{t}}|$, and the absolute value of the rapidity of the leading top-quark jet, and comparisons with the POWHEG+PYTHIA 8 predictions are shown in (a). Data points are placed at the centre of each bin and the POWHEG+PYTHIA 8 predictions are indicated by coloured lines. The measurement and the prediction are shifted by the factors shown in parentheses to aid visibility. The ratios of various MC calculations to the normalized fiducial phase-space differential cross-sections are shown in (b). The dark and light grey bands indicate the total uncertainty and the statistical uncertainty, respectively, of the data in each bin.

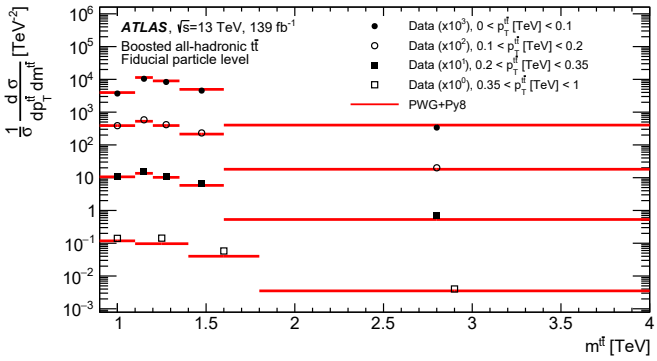

(a)

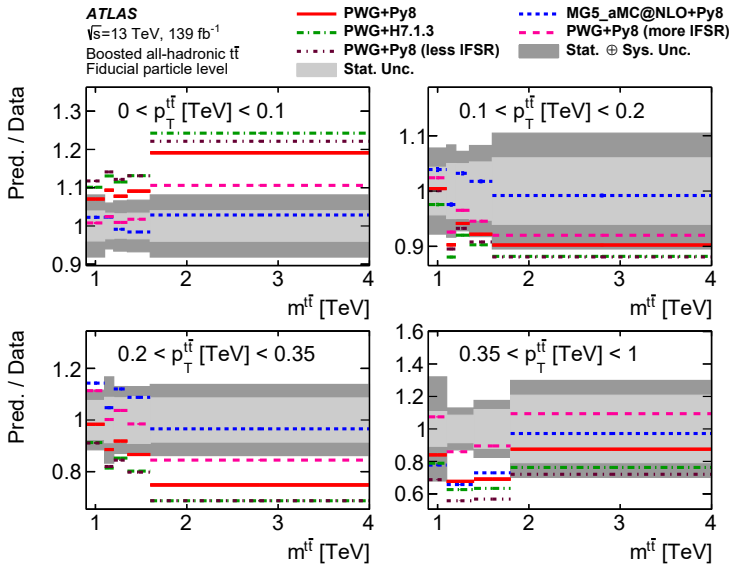

(b)

Figure 18: Normalized particle-level fiducial phase-space double-differential cross-sections as a function of the p_{T} and the mass of the $t\bar{t}$ final state, $p_{\mathrm{T}}^{t\bar{t}}$ and $m^{t\bar{t}}$, and comparisons with the POWHEG+PYTHIA 8 calculation are shown in (a). Data points are placed at the centre of each bin and the POWHEG+PYTHIA 8 calculation are indicated by coloured lines. The measurement and the prediction are normalized by the factors shown in parentheses to aid visibility. The ratios of various MC calculation to the normalized particle-level fiducial phase-space differential cross-sections are shown in (b). The dark and light grey bands indicate the total uncertainty and the statistical uncertainty, respectively, of the data in each bin.

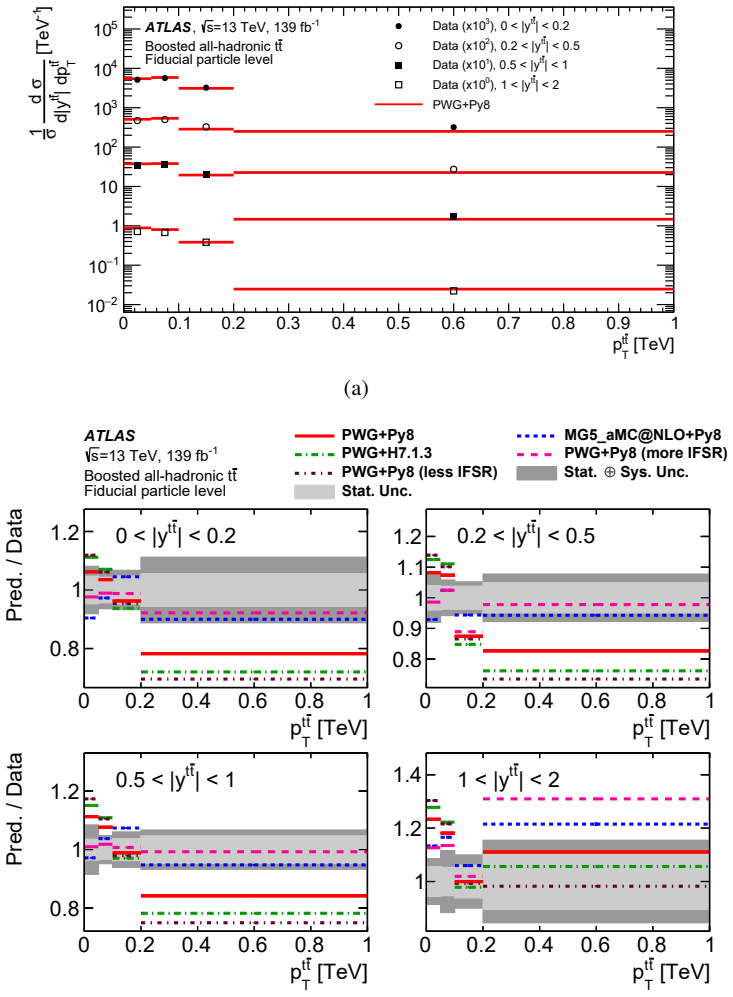

(a)

(b)

Figure 19: Normalized particle-level fiducial phase-space double-differential cross-sections as a function of the absolute value of the rapidity and the p_{T} of the $t\bar{t}$ final state, $\left|y^{t\bar{t}}\right|$ and $p_{\mathrm{T}}^{t\bar{t}}$, and comparisons with the POWHEG+PYTHIA 8 predictions are shown in (a). Data points are placed at the centre of each bin and the POWHEG+PYTHIA 8 predictions are indicated by coloured lines. The measurement and the prediction are normalized by the factors shown in parentheses to aid visibility. The ratios of various MC calculations to the normalized particle-level fiducial phase-space differential cross-sections are shown in (b). The dark and light grey bands indicate the total uncertainty and the statistical uncertainty, respectively, of the data in each bin.

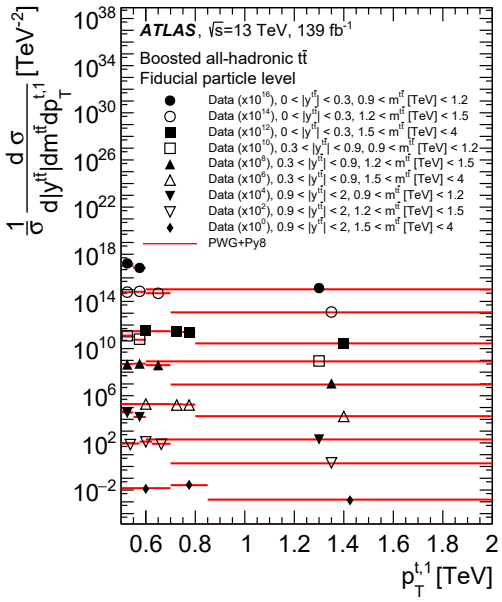

(a)

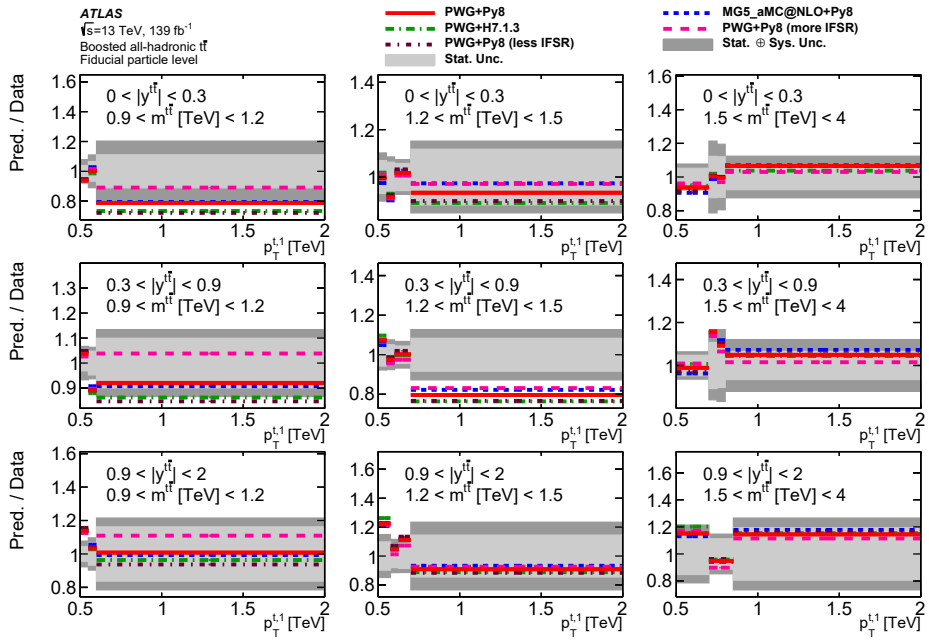

(b)

Figure 20: Normalized particle-level fiducial phase-space triple-differential cross-sections as a function of the absolute value of the rapidity of the $t\bar{t}$ final state, $|y^{t\bar{t}}|$, the mass of the $t\bar{t}$ final state, $m^{t\bar{t}}$, and the p_{T} of the leading top-quark jet are shown in (a). Comparisons are made with the POWHEG+PYTHIA 8 calculations. Data points are placed at the centre of each bin and the POWHEG+PYTHIA 8 predictions are indicated by solid lines. The measurement and the prediction are normalized by the factors shown in parentheses to aid visibility. The ratios of various MC calculations to the normalized particle-level fiducial phase-space differential cross-sections are shown in (b). The dark and light grey bands indicate the total uncertainty and the statistical uncertainty, respectively, of the data in each bin.

9.3 Total parton-level cross-section in the fiducial phase-space

The measurement of the parton-level fiducial phase-space cross-section is performed as a single-bin unfolding to the parton-level phase space. This results in

$$\sigma_{\text{parton}}^{t\bar{t},\text{fid}} = 1.94 \pm 0.02(\text{stat.}) \pm 0.25(\text{syst.}) \text{ pb},$$

where a correction has been made for the $t\bar{t}$ branching fraction to the all-hadronic final state.

The measured cross-section can be compared with the cross-section calculation of 2.34 ± 0.28 pb by the Powheg+Pythia 8 calculation after normalizing its full phase-space calculation to the NNLO+NNLL $t\bar{t}$ cross-section. It can be also compared with the nominal fixed-order NNLO cross-section calculation of $1.96^{+0.02}_{-0.17}$ pb obtained using the Matrix program, described in Section 3. The Powheg+Pythia 8 associated uncertainty includes the statistical, scale, PDF, and NNLO+NNLL total inclusive calculation uncertainty, while the NNLO calculation includes the scale uncertainties, which are highly asymmetric, and the statistical uncertainties. Figure 21 compares the measured parton-level cross-section with various MC NLO calculations and also with the fixed-order NNLO calculation for various PDF sets and dynamical scales.

The difference between the particle-level and parton-level total cross-sections stems mainly from correcting the parton-level cross-section for the $t\bar{t}$ branching fraction to the all-hadronic final state, the particle-level requirements on the leading and second-leading large-R jet masses, and the matching of b-hadrons to large-R jets.

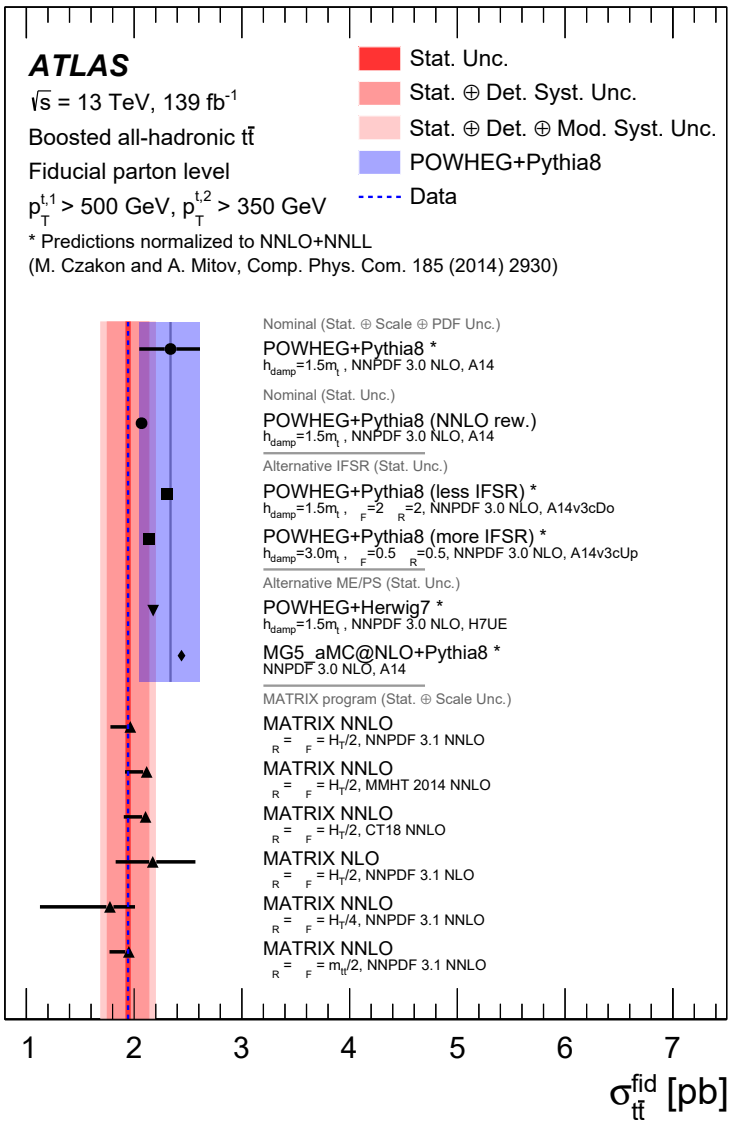

Figure 21: Comparison of the parton-level fiducial phase-space cross-section with the calculations from several MC generators and the fixed-order NNLO prediction with various PDF sets and dynamical scales obtained using the MATRIX program. A correction has been made for the $t\bar{t}$ branching fraction to the all-hadronic final state. The shaded (red) bands indicate the statistical, detector, and modelling uncertainties in the measurement. The uncertainty associated with the POWHEG+PYTHIA 8 signal model (blue band) includes the statistical, scale, PDF, and NNLO+NNLL total inclusive prediction uncertainty. Other MC calculations show only the statistical uncertainty of the MC calculation, which is negligible and not visible in the figure. The fixed-order NNLO calculations include the scale uncertainties, which are highly asymmetric, and the statistical uncertainties.

9.4 Parton-level differential cross-sections

The normalized parton-level fiducial phase-space differential cross-section distributions are compared with SM predictions in Figures 22–24: the differential cross-sections that probe the p_{T} of the top quarks and the invariant mass of the $t\bar{t}$ system (Figure 22), the rapidity of top quarks and of the $t\bar{t}$ system (Figure 23), and the extra radiation from the $t\bar{t}$ system (Figure 24). The remaining distributions are presented in Appendix B.

A selection of the fiducial phase-space double- and triple-differential cross-sections are shown in Figures 25–32. Other double- and triple-differential cross-sections are presented in Appendix B.

Figure 33 shows the ratio of calculation to data for differential cross-sections in $p_{\mathrm{T}}^{t,1}$ and $p_{\mathrm{T}}^{t\bar{t}}$. Ratios are shown for various fixed-order calculations at NLO and NNLO together with the nominal POWHEG+PYTHIA 8 calculation. The fixed-order predictions are plotted with the scale uncertainties, which are highly asymmetric.

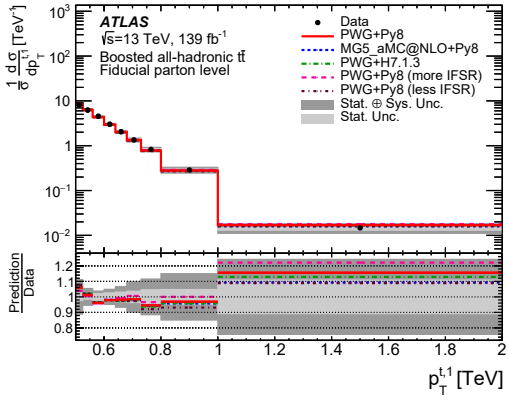

(a)

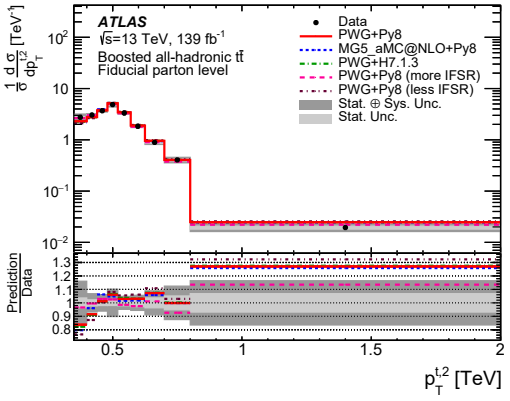

(b)

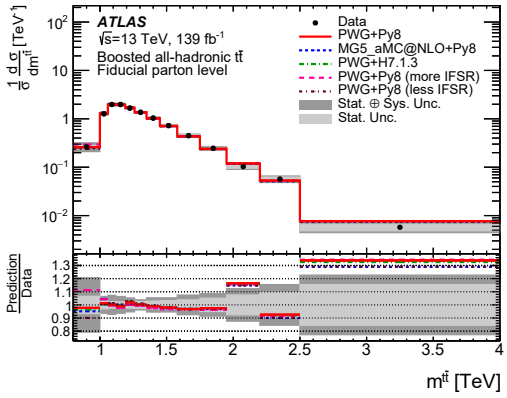

(c)

Figure 22: The normalized parton-level fiducial phase-space differential cross-sections as a function of (a) the p_{T} of the leading top quark, (b) the p_{T} of the second-leading top quark, and (c) the invariant mass of the $t\bar{t}$ system, $m^{t\bar{t}}$. The dark and light grey bands indicate the total uncertainty and the statistical uncertainty, respectively, of the data in each bin. Data points are placed at the centre of each bin. The POWHEG+PYTHIA 8 MC sample is used as the nominal calculations to correct the data to parton level.

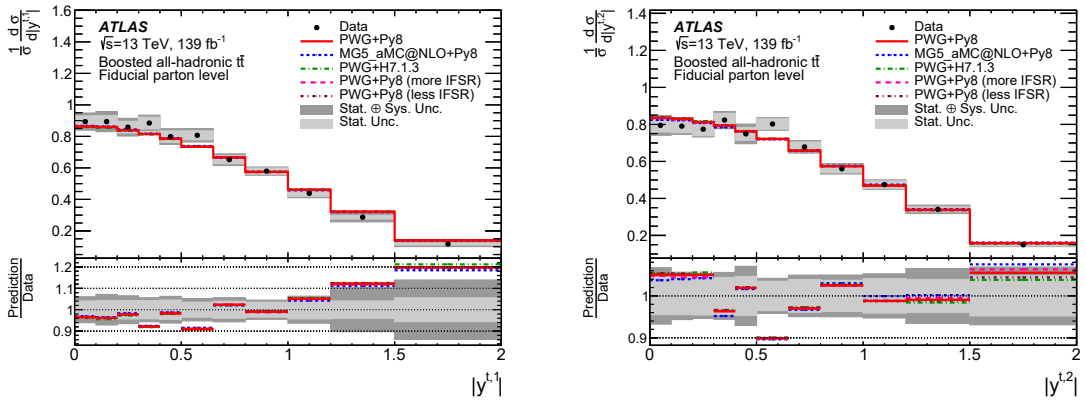

(a) (b)

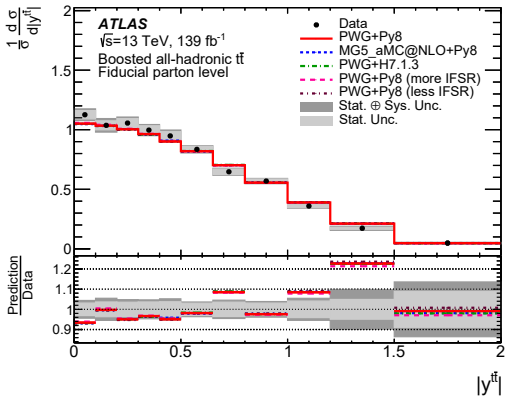

(c)

Figure 23: The normalized parton-level fiducial phase-space differential cross-sections as a function of the absolute value of the rapidity of (a) the leading top quark, (b) the second-leading top quark, and (c) the $t\bar{t}$ system, $|y^{t\bar{t}}|$. The dark and light grey bands indicate the total uncertainty and the statistical uncertainty, respectively, of the data in each bin. Data points are placed at the centre of each bin. The POWHEG+PYTHIA 8 MC sample is used as the nominal calculations to correct the data to parton level.

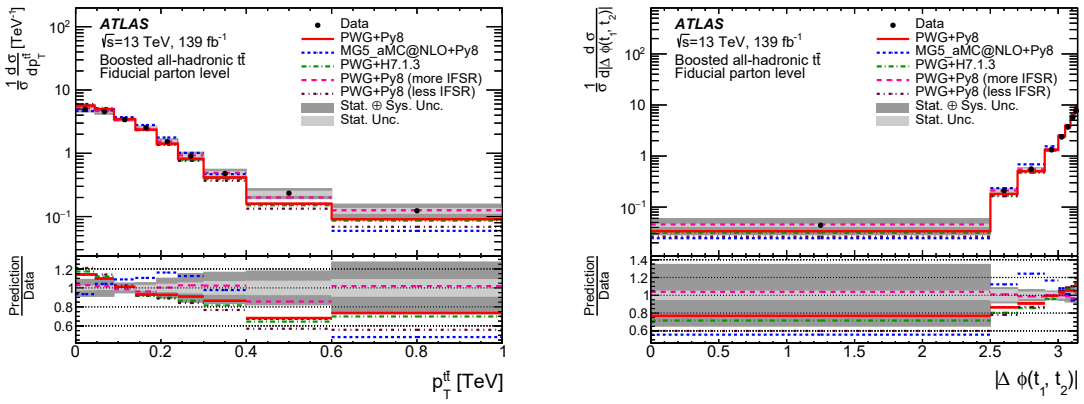

(a) (b)

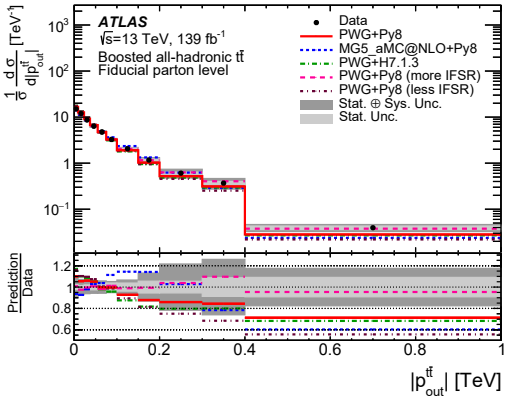

(c)

Figure 24: The normalized parton-level differential cross-sections as a function of (a) the p_{T} of the $t\bar{t}$ system, $p_{\mathrm{T}}^{t\bar{t}}$, (b) the azimuthal angle between the two top quarks, $\Delta\phi^{t\bar{t}}$, and (c) the absolute value of the out-of-plane momentum, $p_{\mathrm{out}}^{t\bar{t}}$. The dark and light grey bands indicate the total uncertainty and the statistical uncertainty, respectively, of the data in each bin. Data points are placed at the centre of each bin. The Powheg+Pythia 8 MC sample is used as the nominal calculation to correct the data to parton level.

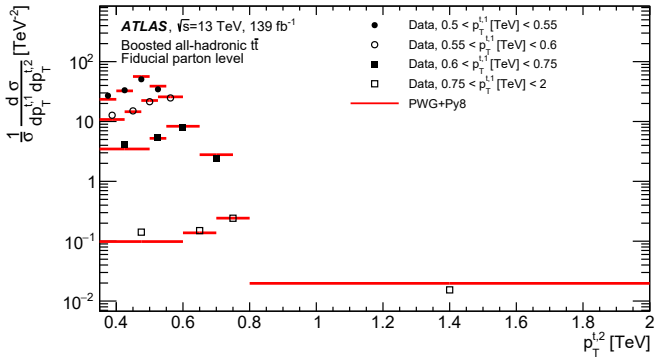

(a)

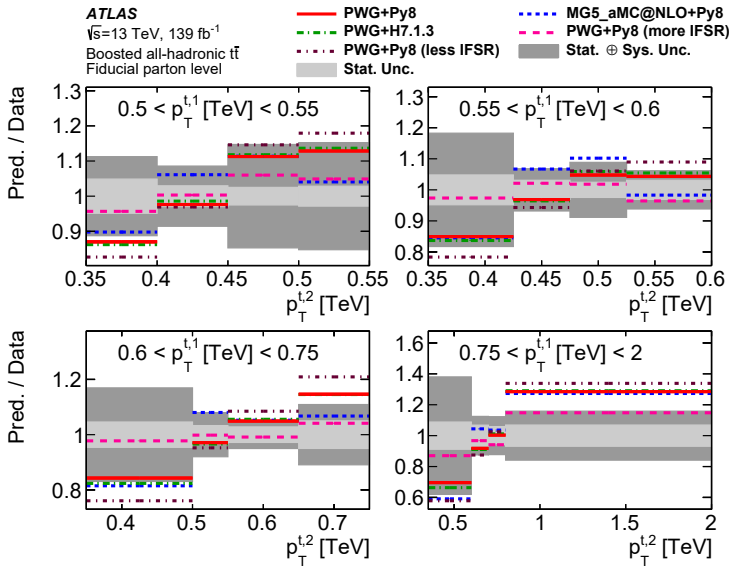

(b)

Figure 25: (a) The normalized parton-level fiducial phase-space double-differential cross-section as a function of the p_{T} of the leading and second-leading top quarks, compared with the POWHEG+PYTHIA 8 calculation. Data points are placed at the centre of each bin and the POWHEG+PYTHIA 8 calculation are indicated by coloured lines. (b) The ratio of various MC calculations to the measured differential cross-sections. The dark and light grey bands indicate the total uncertainty and the statistical uncertainty, respectively, of the data in each bin.

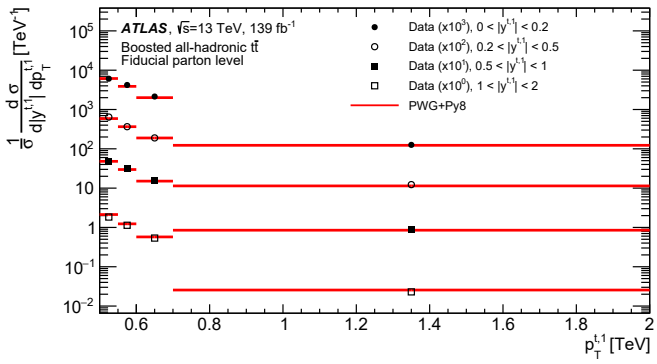

(a)

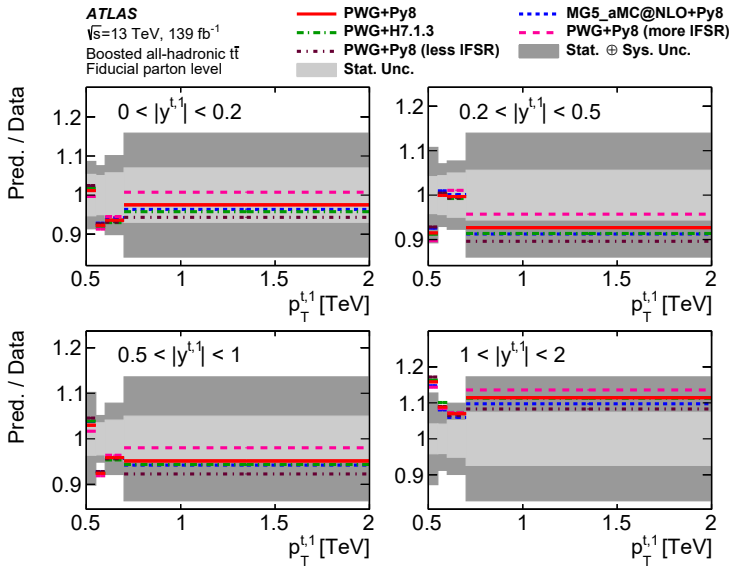

(b)

Figure 26: (a) The normalized parton-level fiducial phase-space double-differential cross-section as a function of the absolute value of the leading top-quark rapidity and p_{T}, compared with the Powheg+Pythia 8 calculation. Data points are placed at the centre of each bin and the Powheg+Pythia 8 predictions are indicated by solid lines. The measurement and the prediction are normalized by the factors shown in parentheses to aid visibility. (b) The ratios of various MC calculations to the measured differential cross-sections. The dark and light grey bands indicate the total uncertainty and the statistical uncertainty, respectively, of the data in each bin.

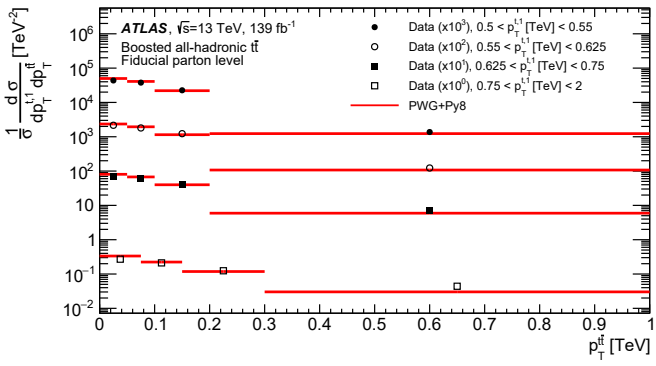

(a)

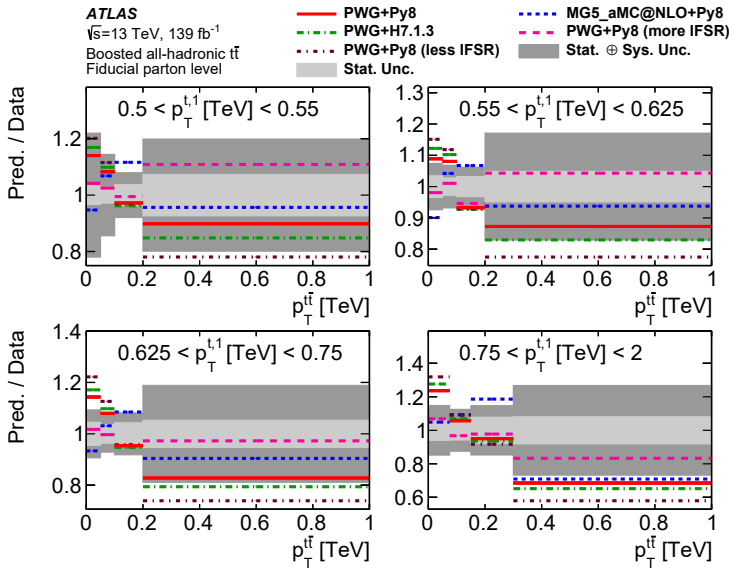

(b)

Figure 27: (a) The normalized parton-level fiducial phase-space double-differential cross-section as a function of the p_{T} of the leading top quark and the transverse momentum of the $t\bar{t}$ system, $p_{\mathrm{T}}^{t\bar{t}}$, compared with the POWHEG+PYTHIA 8 calculation. Data points are placed at the centre of each bin and the POWHEG+PYTHIA 8 predictions are indicated by solid lines. The measurement and the prediction are normalized by the factors shown in parentheses to aid visibility. (b) The ratios of various MC calculations to the measured differential cross-sections. The dark and light grey bands indicate the total uncertainty and the statistical uncertainty, respectively, of the data in each bin.

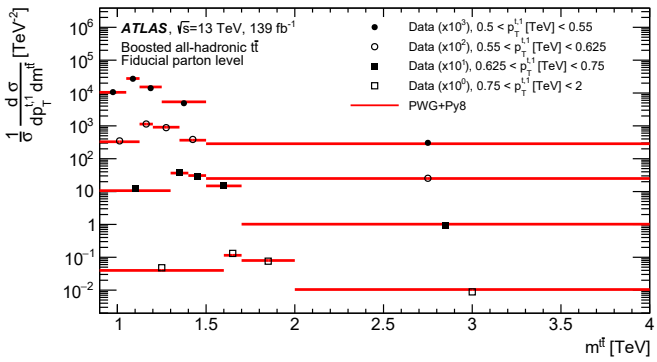

(a)

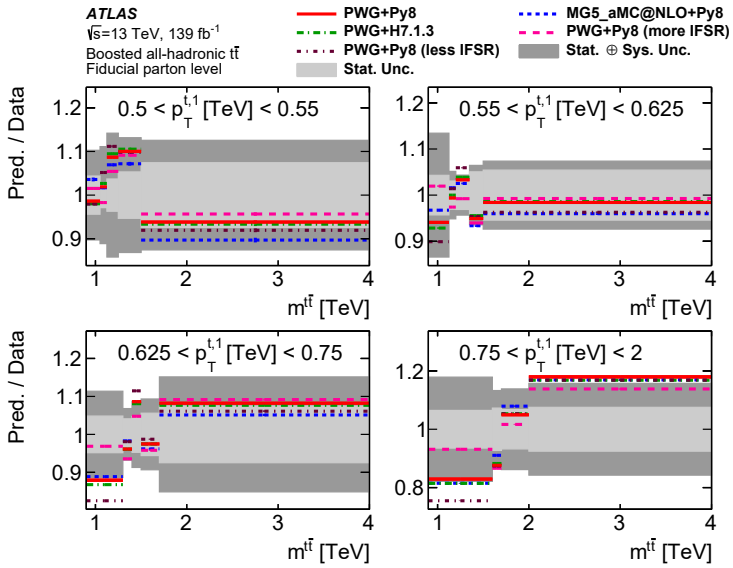

(b)

Figure 28: (a) The normalized parton-level fiducial phase-space double-differential cross-section as a function of the p_{T} of the leading top quark and the invariant mass of the $t\bar{t}$ system, $m^{t\bar{t}}$, compared with the POWHEG+PYTHIA 8 calculation. Data points are placed at the centre of each bin and the POWHEG+PYTHIA 8 predictions are indicated by solid lines. The measurement and the prediction are normalized by the factors shown in parentheses to aid visibility. (b) The ratios of various MC calculations to the measured differential cross-sections. The dark and light grey bands indicate the total uncertainty and the statistical uncertainty, respectively, of the data in each bin.

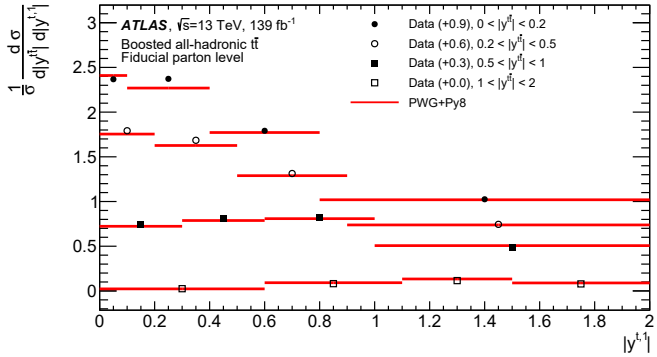

(a)

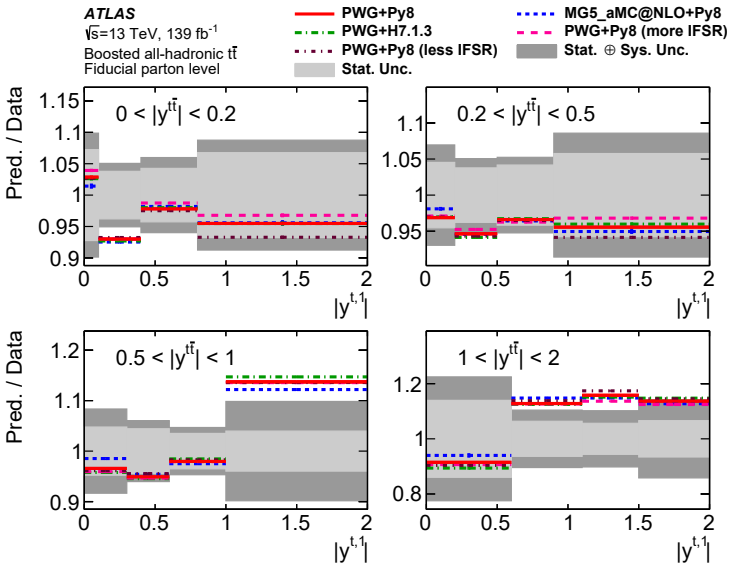

(b)

Figure 29: (a) The normalized parton-level fiducial phase-space double-differential cross-section as a function of the absolute value of the rapidity of the $t\bar{t}$ system, $|y^{t\bar{t}}|$, and the rapidity of the leading top quark compared with the POWHEG+PYTHIA 8 calculation. Data points are placed at the centre of each bin and the POWHEG+PYTHIA 8 predictions are indicated by solid lines. The measurement and the prediction are shifted by the factors shown in parentheses to aid visibility. (b) The ratios of various MC calulations to the measured differential cross-sections. The dark and light grey bands indicate the total uncertainty and the statistical uncertainty, respectively, of the data in each bin.

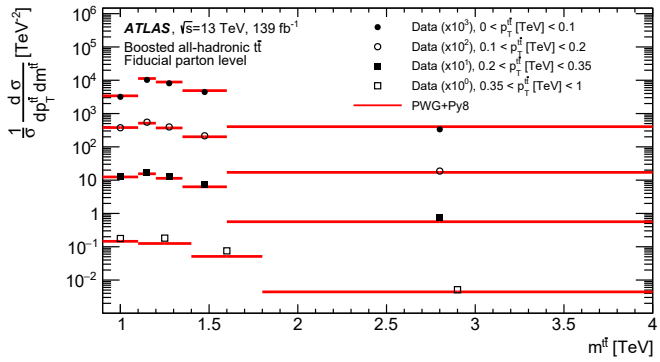

(a)

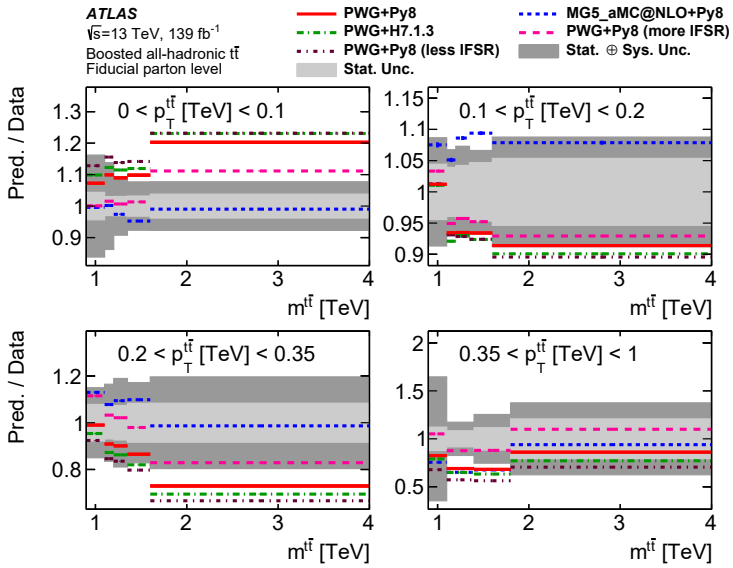

(b)

Figure 30: (a) The normalized parton-level fiducial phase-space double-differential cross-section as a function of the p_{T} and the mass of the $t\bar{t}$ system, $p_{\mathrm{T}}^{t\bar{t}}$ and $m^{t\bar{t}}$, compared with the Powheg+Pythia 8 calculation. Data points are placed at the centre of each bin and the Powheg+Pythia 8 predictions are indicated by solid lines. The measurement and the prediction are normalized by the factors shown in parentheses to aid visibility. (b) The ratios of various MC calculations to the measured differential cross-sections. The dark and light grey bands indicate the total uncertainty and the statistical uncertainty, respectively, of the data in each bin.

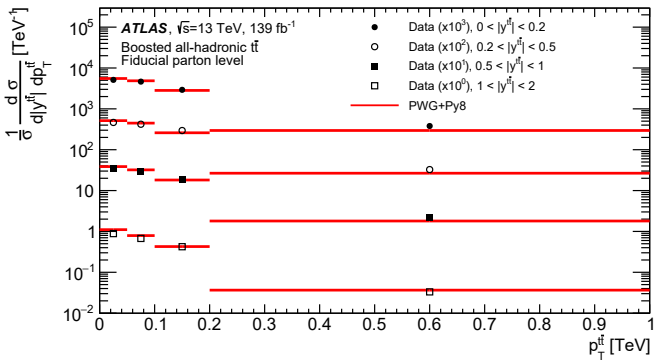

(a)

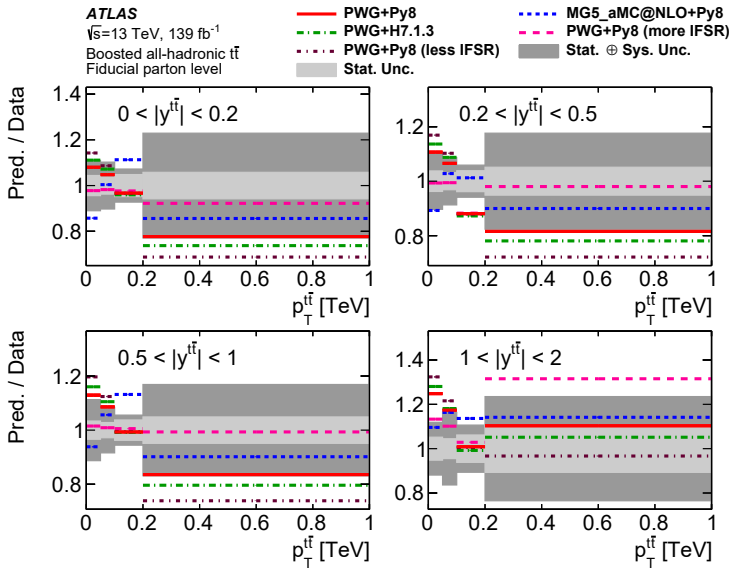

(b)

Figure 31: (a) The normalized parton-level fiducial phase-space double-differential cross-section as a function of the absolute value of the rapidity and the p_{T} of the $t\bar{t}$ system, $|y^{t\bar{t}}|$ and $p_{\mathrm{T}}^{t\bar{t}}$, compared with the Powheg+Pythia 8 calculation. Data points are placed at the centre of each bin and the Powheg+Pythia 8 predictions are indicated by solid lines. The measurement and the prediction are normalized by the factors shown in parentheses to aid visibility. (b) The ratios of various MC calculations to the measured differential cross-sections. The dark and light grey bands indicate the total uncertainty and the statistical uncertainty, respectively, of the data in each bin.

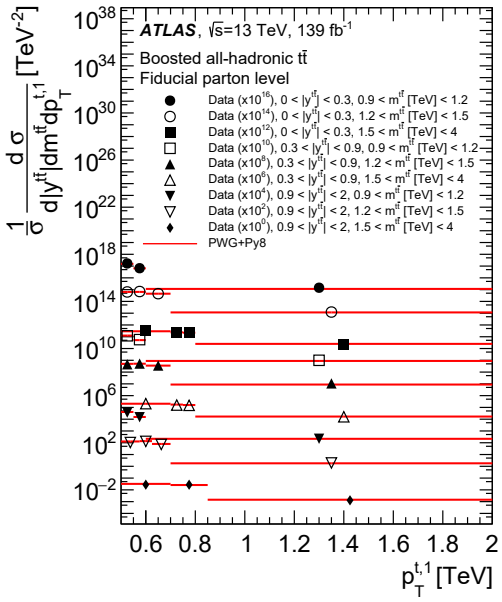

(a)

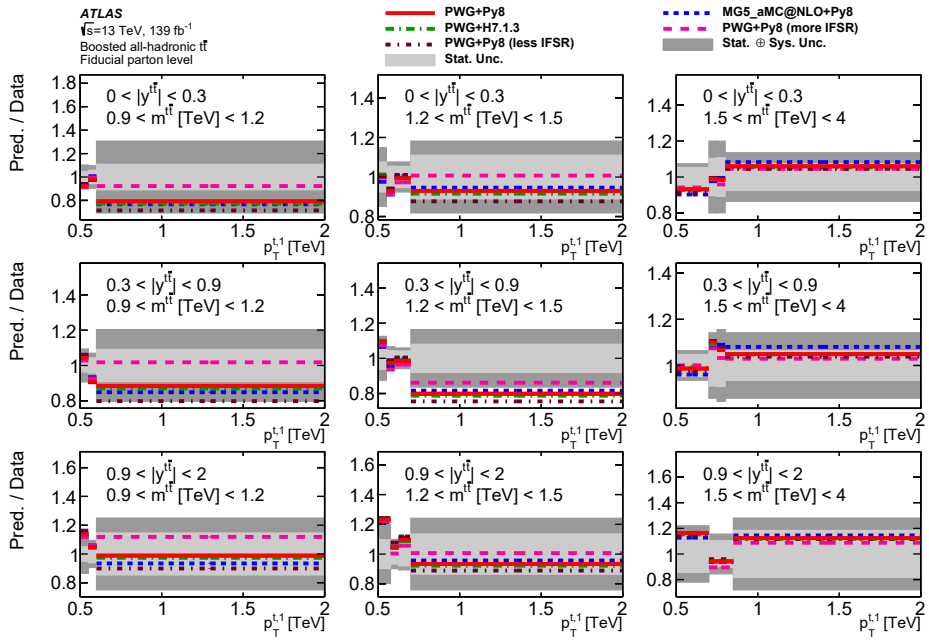

(b)

Figure 32: (a) The normalized parton-level fiducial phase-space triple-differential cross-section as a function of the absolute value of the rapidity and the mass of the $t\bar{t}$ system, $\left|y^{t\bar{t}}\right|$ and $p_{\mathrm{T}}^{t\bar{t}}$, and the p_{T} of the leading top quark, compared with the POWHEG+PYTHIA 8 calculations. Data points are placed at the centre of each bin and the POWHEG+PYTHIA 8 predictions are indicated by solid lines. The measurement and the prediction are normalized by the factors shown in parentheses to aid visibility. (b) The ratios of various MC calculations to the measured differential cross-sections. The dark and light grey bands indicate the total uncertainty and the statistical uncertainty, respectively, of the data in each bin.

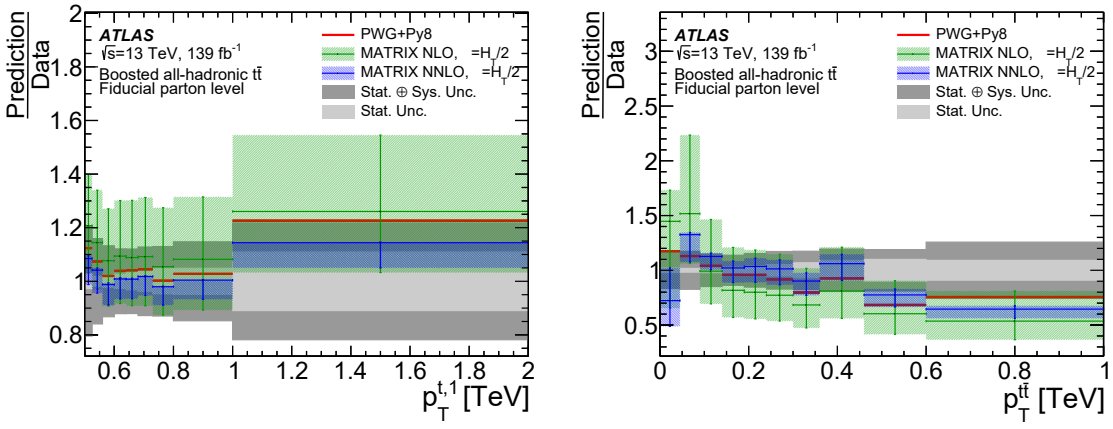

(a) (b)

Figure 33: Comparison of the NLO, NNLO, and POWHEG+PYTHIA 8 calculations with measured parton-level fiducial phase-space absolute differential cross-sections for (a) the p_{T} of the leading top quark, and (b) the p_{T} of the $t\bar{t}$ system, $p_{\mathrm{T}}^{t\bar{t}}$. The dark and light grey bands indicate the total uncertainty and the statistical uncertainty, respectively, of the data in each bin. The fixed-order calculation bands correspond to the scale uncertainty.

10 Comparisons with QCD calculations

The nominal POWHEG+PYTHIA 8 particle-level and parton-level cross-sections for top-quark pair production in their corresponding fiducial phase-space regions are 20% larger than the observed values as shown in Figure 9 and Figure 21, respectively. The significance of this difference is $\sim 1.1\sigma$ when taking into account both the uncertainties of the measurements and the corresponding uncertainties in the POWHEG+PYTHIA 8 predictions. At both the particle level and parton level, there is better agreement with the POWHEG+HERWIG 7.1.3 calculations and the predictions of POWHEG+PYTHIA 8 with increased initial- and final-state radiation, where the differences correspond to ~0.5 standard deviations. Agreement with the nominal POWHEG+PYTHIA 8 calculation improves after reweighting those to the NNLO calculation. At parton level, even better agreement with the NNLO MATRIX calculation is observed for various definitions of the renormalization and factorization scales, as well as for different PDF sets. This is consistent with previous measurements that have observed that the top-quark p_{T} spectra are softer than in various NLO+PS predictions at high top-quark p_{T} [8–11, 13–15].

The particle-level fiducial phase-space differential cross-sections and the parton-level differential cross-sections are compared with several SM predictions. In this comparison, there are no uncertainties associated with the predictions. The information provided by the shapes of the differential cross-section measurements is compared with the calculations using the χ^2 test described in Section 8.2, which takes into account the correlations between the measured quantities while the uncertainty in the prediction is not included. The largest correlations at the detector level arise from sources of uncertainty that affect all bins equally. The most sensitive comparison uses the normalized differential cross-sections because many of the common detector-level uncertainties largely cancel out. The χ^2 values and associated p-values are shown in Table 4 and Table 5 for the normalized particle-level and parton-level fiducial phase-space differential cross-sections, respectively. No comparison with the fixed-order NNLO calculation is shown because numerical instabilities were observed in certain phase-space regions (e.g. around $p_{\mathrm{T}}^{t\bar{t}} \sim 0$).

Observable	PWG+Py8 NNPDF30 A14		MG5_aMC@NLO+Py8 NNPDF30 UE-EE-5		PWG+H7.1.3 NNPDF30 A14		PWG+Py8 (more IFSR) NNPDF30 A14		PWG+Py8 (less IFSR) NNPDF30 A14	
	χ^2/NDF	p-value	χ^2/NDF	p-value	χ^2/NDF	p-value	χ^2/NDF	p-value	χ^2/NDF	p-value
p_{T}^{t}	3.9/9	0.92	3.1/9	0.96	6.2/9	0.72	1.2/9	1.00	7.7/9	0.57
$\lvert y^{t}\rvert$	6.8/10	0.75	5.8/10	0.83	6.8/10	0.74	7.5/10	0.68	5.9/10	0.83
$p_{\mathrm{T}}^{t,1}$	5.1/8	0.75	3.9/8	0.86	5.3/8	0.72	4.3/8	0.83	5.3/8	0.72
$\lvert y^{t,1}\rvert$	6.1/10	0.81	4.7/10	0.91	6.7/10	0.76	5.7/10	0.84	5.6/10	0.84
$p_{\mathrm{T}}^{t,2}$	9.9/8	0.27	10.2/8	0.25	13.9/8	0.08	4.4/8	0.82	16.0/8	0.04
$\lvert y^{t,2}\rvert$	9.4/10	0.49	9.0/10	0.53	9.4/10	0.50	8.9/10	0.54	9.3/10	0.50
$m^{t\bar{t}}$	8.1/12	0.78	6.9/12	0.87	7.4/12	0.83	8.9/12	0.71	7.9/12	0.79
$p_{\mathrm{T}}^{t\bar{t}}$	14.3/8	0.07	35.2/8	< 0.01	24.5/8	< 0.01	2.7/8	0.95	33.5/8	< 0.01
$\lvert y^{t\bar{t}}\rvert$	16.7/10	0.08	17.3/10	0.07	18.1/10	0.05	14.8/10	0.14	17.9/10	0.06
$\chi^{t\bar{t}}$	8.0/11	0.71	10.0/11	0.53	8.1/11	0.71	9.5/11	0.57	12.4/11	0.34
$\lvert y_{\mathrm{B}}^{t\bar{t}}\rvert$	15.3/10	0.12	15.7/10	0.11	16.6/10	0.08	14.1/10	0.17	16.6/10	0.08
$\lvert p_{\mathrm{out}}^{t\bar{t}}\rvert$	17.1/10	0.07	53.6/10	< 0.01	30.9/10	< 0.01	8.6/10	0.57	32.7/10	< 0.01
$H_{\mathrm{T}}^{t\bar{t}}$	5.4/9	0.80	5.0/9	0.83	6.4/9	0.70	3.6/9	0.94	6.8/9	0.66
$\lvert\Delta\phi(t_1,t_2)\rvert$	12.2/7	0.09	73.4/7	< 0.01	23.6/7	< 0.01	5.3/7	0.63	28.5/7	< 0.01
$\lvert\cos\theta^{\star}\rvert$	7.0/10	0.72	9.8/10	0.46	6.8/10	0.74	7.4/10	0.69	10.5/10	0.39
$p_{\mathrm{T}}^{t,1} \otimes p_{\mathrm{T}}^{t,2}$	27.1/15	0.03	27.0/15	0.03	36.7/15	< 0.01	12.0/15	0.68	41.0/15	< 0.01
$\lvert y^{t,1}\rvert \otimes \lvert y^{t,2}\rvert$	11.6/19	0.90	9.8/19	0.96	12.0/19	0.88	14.3/19	0.77	9.7/19	0.96
$\lvert y^{t,1}\rvert \otimes p_{\mathrm{T}}^{t,1}$	8.5/15	0.90	7.6/15	0.94	9.4/15	0.85	9.5/15	0.85	8.4/15	0.91
$\lvert y^{t,2}\rvert \otimes p_{\mathrm{T}}^{t,2}$	15.9/20	0.72	17.1/20	0.65	19.5/20	0.49	10.8/20	0.95	20.7/20	0.41
$p_{\mathrm{T}}^{t,1} \otimes p_{\mathrm{T}}^{t\bar{t}}$	16.1/15	0.37	12.6/15	0.63	26.7/15	0.03	7.3/15	0.95	30.7/15	< 0.01
$p_{\mathrm{T}}^{t,1} \otimes m^{t\bar{t}}$	23.1/18	0.19	21.9/18	0.24	26.7/18	0.08	13.8/18	0.74	30.5/18	0.03
$\lvert y^{t\bar{t}}\rvert \otimes p_{\mathrm{T}}^{t,1}$	14.4/15	0.50	14.5/15	0.49	15.0/15	0.45	12.8/15	0.62	15.6/15	0.41
$\lvert y^{t\bar{t}}\rvert \otimes \lvert y^{t,1}\rvert$	14.7/15	0.47	18.0/15	0.26	15.6/15	0.41	11.6/15	0.71	19.1/15	0.21
$\lvert y^{t,1}\rvert \otimes m^{t\bar{t}}$	20.0/19	0.40	20.1/19	0.39	20.0/19	0.39	19.5/19	0.42	20.3/19	0.38
$\lvert y^{t\bar{t}}\rvert \otimes m^{t\bar{t}}$	12.5/18	0.82	12.1/18	0.84	13.2/18	0.78	12.5/18	0.82	12.9/18	0.80
$p_{\mathrm{T}}^{t\bar{t}} \otimes m^{t\bar{t}}$	20.2/18	0.32	17.9/18	0.46	30.9/18	0.03	9.4/18	0.95	35.2/18	< 0.01
$\lvert y^{t\bar{t}}\rvert \otimes p_{\mathrm{T}}^{t\bar{t}}$	19.1/15	0.21	14.5/15	0.49	29.4/15	0.01	12.2/15	0.66	33.4/15	< 0.01
$\lvert y^{t\bar{t}}\rvert \otimes m^{t\bar{t}} \otimes p_{\mathrm{T}}^{t,1}$	21.9/31	0.88	24.1/31	0.81	24.6/31	0.79	18.0/31	0.97	26.9/31	0.68

Table 4: Comparison between the measured normalized particle-level fiducial phase-space differential cross-sections and the predictions of several MC event generators. For each observed and predicted differential cross-section, a χ^2 and a p-value are calculated using the covariance matrix described in the text, which includes all sources of uncertainty in the measurement. The uncertainty in the prediction is not included. The number of degrees of freedom (NDF) is equal to $N_{\mathrm{b}} - 1$, where N_{b} is the number of measured values in the distribution.

In the case of the normalized particle-level fiducial phase-space differential cross-sections, good agreement is generally observed. The one-dimensional distributions that are sensitive to extra radiation (i.e. the p_{T} of the $t\bar{t}$ system, $p_{\mathrm{T}}^{t\bar{t}}$, the out-of-plane momentum, $\left|p_{\mathrm{out}}^{t\bar{t}}\right|$, and the absolute value of the azimuthal separation of the top-quark jets, $\left|\Delta\phi^{t\bar{t}}\right|$) yield p-values below 1% for all MC predictions except for the nominal prediction of Powheg+Pythia 8 and those including more initial- and final-state radiation. These distributions indicate a deficit of radiation in the MC predictions, i.e. $p_{\mathrm{T}}^{t\bar{t}}$ (Figure 12(a)) and $p_{\mathrm{out}}^{t\bar{t}}$ (Figure 12(c)) are softer, while $\left|\Delta\phi^{t\bar{t}}\right|$ (Figure 12(b)) is closer to π for the predictions. Moreover, the aMC@NLO+Pythia 8 calculations for these observables differ significantly from the predictions of the other MC generators. It is notable that these discrepancies are not evident in the parton-level comparisons.

The $p_{\mathrm{T}}^{t,2}$ distribution (Figure 10(b)), and consequently $H_{\mathrm{T}}^{t\bar{t}}$ to a lesser extent (Figure 38(a)), indicates that the MC particle-level predictions have a harder $p_{\mathrm{T}}^{t\bar{t}}$ distribution than is observed in data, except for the prediction of Powheg+Pythia 8 with more initial- and final-state radiation. Low p-values are seen for the comparison of the multi-dimensional distributions for $p_{\mathrm{T}}^{t,1} \otimes p_{\mathrm{T}}^{t,2}$ (Figure 13) for all MC calculations except for the prediction of Powheg+Pythia 8 with more initial- and final-state radiation. The largest slope in the calculation/data ratio is observed for the largest values of $p_{\mathrm{T}}^{t,1}$. The Powheg+Herwig 7.1.3 calculations and the calculations of Powheg+Pythia 8 with less initial- and final-state radiation give low p-values for the $p_{\mathrm{T}}^{t,1} \otimes p_{\mathrm{T}}^{t\bar{t}}$ (Figure 15), $p_{\mathrm{T}}^{t\bar{t}} \otimes m^{t\bar{t}}$ (Figure 18) and $\left|y^{t\bar{t}}\right| \otimes p_{\mathrm{T}}^{t\bar{t}}$ (Figure 19) distributions. There are large slopes in the calculation/data ratios for all $p_{\mathrm{T}}^{t,1} \otimes p_{\mathrm{T}}^{t\bar{t}}$ (Figure 15) and $\left|y^{t\bar{t}}\right| \otimes p_{\mathrm{T}}^{t\bar{t}}$ (Figure 19) distributions,

Observable	PWG+Py8 NNPDF30 A14		MG5_aMC@NLO+Py8 NNPDF30 UE-EE-5		PWG+H7.1.3 NNPDF30 A14		PWG+Py8 (more IFSR) NNPDF30 A14		PWG+Py8 (less IFSR) NNPDF30 A14	
	χ^2/NDF	p-value	χ^2/NDF	p-value	χ^2/NDF	p-value	χ^2/NDF	p-value	χ^2/NDF	p-value
p_{T}^{t}	3.1/9	0.96	3.7/9	0.93	4.3/9	0.89	1.4/9	1.00	6.2/9	0.72
$\lvert y^{t}\rvert$	6.2/10	0.80	6.1/10	0.81	6.0/10	0.82	6.1/10	0.80	5.8/10	0.83
$p_{\mathrm{T}}^{t,1}$	3.2/8	0.92	2.6/8	0.96	3.6/8	0.89	4.0/8	0.86	3.1/8	0.93
$\lvert y^{t,1}\rvert$	5.7/10	0.84	5.0/10	0.89	5.9/10	0.82	5.5/10	0.86	5.5/10	0.86
$p_{\mathrm{T}}^{t,2}$	5.4/8	0.71	9.6/8	0.30	5.9/8	0.66	3.2/8	0.92	8.3/8	0.41
$\lvert y^{t,2}\rvert$	9.3/10	0.51	9.6/10	0.48	9.2/10	0.51	9.1/10	0.52	9.2/10	0.52
$m^{t\bar{t}}$	7.4/12	0.83	8.6/12	0.73	7.4/12	0.83	7.6/12	0.81	7.1/12	0.85
$p_{\mathrm{T}}^{t\bar{t}}$	7.2/8	0.51	23.5/8	< 0.01	8.6/8	0.38	3.1/8	0.93	13.0/8	0.11
$\lvert y^{t\bar{t}}\rvert$	13.1/10	0.22	13.5/10	0.20	13.6/10	0.19	12.1/10	0.28	13.9/10	0.18
$\chi^{t\bar{t}}$	7.6/11	0.74	8.0/11	0.71	8.3/11	0.69	7.4/11	0.77	9.9/11	0.54
$\lvert y_{\mathrm{B}}^{t\bar{t}}\rvert$	11.7/10	0.31	12.0/10	0.29	11.7/10	0.31	11.1/10	0.35	12.5/10	0.26
$\lvert p_{\mathrm{out}}^{t\bar{t}}\rvert$	7.1/10	0.72	44.9/10	< 0.01	12.5/10	0.25	4.6/10	0.92	11.2/10	0.34
$H_{\mathrm{T}}^{t\bar{t}}$	3.4/9	0.95	3.3/9	0.95	3.8/9	0.93	3.3/9	0.95	3.7/9	0.93
$\lvert\Delta\phi(t_1,t_2)\rvert$	10.5/7	0.16	81.1/7	< 0.01	25.9/7	< 0.01	4.2/7	0.76	19.2/7	< 0.01
$\lvert\cos\theta^{\star}\rvert$	7.1/10	0.72	7.8/10	0.65	7.5/10	0.67	6.6/10	0.76	8.6/10	0.57
$p_{\mathrm{T}}^{t,1} \otimes p_{\mathrm{T}}^{t,2}$	13.7/15	0.55	23.2/15	0.08	16.5/15	0.35	5.8/15	0.98	22.5/15	0.10
$\lvert y^{t,1}\rvert \otimes \lvert y^{t,2}\rvert$	9.8/15	0.83	9.6/15	0.85	9.5/15	0.85	10.3/15	0.80	9.2/15	0.86
$\lvert y^{t,1}\rvert \otimes p_{\mathrm{T}}^{t,1}$	8.0/15	0.92	7.5/15	0.94	8.6/15	0.90	8.8/15	0.89	8.1/15	0.92
$\lvert y^{t,2}\rvert \otimes p_{\mathrm{T}}^{t,2}$	13.5/20	0.86	15.7/20	0.74	13.5/20	0.86	11.3/20	0.94	16.5/20	0.68
$p_{\mathrm{T}}^{t,1} \otimes p_{\mathrm{T}}^{t\bar{t}}$	11.9/15	0.69	21.5/15	0.12	15.4/15	0.42	6.9/15	0.96	22.2/15	0.10
$p_{\mathrm{T}}^{t,1} \otimes m^{t\bar{t}}$	17.8/18	0.47	19.5/18	0.36	17.6/18	0.48	12.9/18	0.80	23.8/18	0.16
$\lvert y^{t\bar{t}}\rvert \otimes p_{\mathrm{T}}^{t,1}$	12.0/15	0.68	11.6/15	0.71	11.4/15	0.72	11.5/15	0.71	12.7/15	0.63
$\lvert y^{t\bar{t}}\rvert \otimes \lvert y^{t,1}\rvert$	14.2/15	0.51	14.7/15	0.47	14.1/15	0.52	12.2/15	0.67	17.2/15	0.31
$\lvert y^{t,1}\rvert \otimes m^{t\bar{t}}$	19.0/19	0.46	18.6/19	0.49	19.3/19	0.44	19.0/19	0.46	19.2/19	0.44
$\lvert y^{t\bar{t}}\rvert \otimes m^{t\bar{t}}$	12.3/18	0.83	12.1/18	0.84	12.2/18	0.84	13.6/18	0.75	11.8/18	0.86
$p_{\mathrm{T}}^{t\bar{t}} \otimes m^{t\bar{t}}$	25.9/18	0.10	22.0/18	0.23	32.0/18	0.02	13.8/18	0.74	35.2/18	< 0.01
$\lvert y^{t\bar{t}}\rvert \otimes p_{\mathrm{T}}^{t\bar{t}}$	13.5/15	0.56	18.9/15	0.22	15.6/15	0.41	12.7/15	0.63	16.3/15	0.36
$\lvert y^{t\bar{t}}\rvert \otimes m^{t\bar{t}} \otimes p_{\mathrm{T}}^{t,1}$	15.5/31	0.99	17.9/31	0.97	15.1/31	0.99	15.5/31	0.99	17.7/31	0.97

Table 5: Comparison between the measured normalized parton-level differential cross-sections and the predictions from several MC event generators. For each observable and calculation, a χ^2 and a p-value are calculated using the covariance matrix described in the text, which includes all sources of uncertainty in the measurement. The uncertainty in the calculation is not included. The number of degrees of freedom (NDF) is equal to $N_{\mathrm{b}} - 1$, where N_{b} is the number of bins in the distribution.

which confirm the trends observed in the $p_{\mathrm{T}}^{t\bar{t}}$ differential cross-section, while different trends are observed in different $p_{\mathrm{T}}^{t\bar{t}} \otimes m^{t\bar{t}}$ differential cross-sections (Figure 18). A steep gradient in the calculation/data ratio can also be observed in the $\left|y^{t\bar{t}}\right| \otimes |y^{t,1}|$ (Figure 17) and $p_{\mathrm{T}}^{t,1} \otimes m^{t\bar{t}}$ (Figure 16) differential cross-sections for large values of $\left|y^{t\bar{t}}\right|$ and $p_{\mathrm{T}}^{t,1}$, respectively, for all MC calculations, except for the calculations of Powheg+Pythia 8 with more initial- and final-state radiation.

The level of agreement of the normalized parton-level fiducial phase-space differential cross-section calculations with the measurements is generally better, as evidenced by the differential cross-section comparisons and confirmed by the p-values in Table 5. The better agreement at the parton level, especially in the differential cross-sections as a function of $p_{\mathrm{T}}^{t\bar{t}}$, $\left|p_{\mathrm{out}}^{t\bar{t}}\right|$, and $\left|\Delta\phi^{t\bar{t}}\right|$, suggests that the poorer descriptions at the particle level are introduced by parton-showering and hadronization models, and/or ISR/FSR modelling.

11 EFT interpretation

The SMEFT [50] provides a theoretically elegant way to encode the modifications of the top-quark properties induced by a wide class of BSM theories that reduce to the SM at low energies. Within

the mathematical language of the SMEFT relevant to top-quark physics, the effects of BSM dynamics characterized by an energy scale Λ at which BSM effects become apparent and well above the typical scale for top-quark processes given by m_{top} can be parameterized at low energies, $E \ll \Lambda$, in terms of higher-dimensional operators built from the SM fields while respecting symmetries of the SM such as gauge invariance using the Lagrangian

$$\mathcal{L}_{\text{SMEFT}} = \mathcal{L}_{\text{SM}} + \sum_i \frac{C_i}{\Lambda^2} O_i^{(6)} + \sum_j \frac{B_j}{\Lambda^4} O_j^{(8)} + ..., \tag{3}$$

where $\mathcal{L}_{\text{SM}}$ is the SM Lagrangian, $O_i^{(6)}$ and $O_j^{(8)}$ represent a complete set of operators of mass-dimensions $d = 6$ and $d = 8$, and C_i and B_j are the corresponding complex-valued Wilson coefficients that determine the strength of the operators. Operators with $d = 5$ and $d = 7$ violate lepton and/or baryon number conservation and are not relevant for top-quark physics. The effective-theory expansion in Eq. (3) is robust, fully general, and can be systematically matched to explicit ultraviolet-complete BSM scenarios. Contributions from operators of mass-dimension $d = 8$ or higher are not considered in this analysis.

Measurements of top-quark differential cross-sections can place constraints on SMEFT Wilson coefficients. For any cross-section $\sigma(C_i)$, the corresponding expression including SM and SMEFT operators up to dimension-6 becomes

$$\begin{aligned} \sigma(C_i) &= \sigma_{\text{SM}} + \sigma_{\text{SM–EFT}} + \sigma_{\text{EFT–EFT}} \\ &= \sigma_{\text{SM}} + \frac{1}{\Lambda^2} \sum_i \alpha_i C_i + \frac{1}{\Lambda^4} \sum_i \beta_i C_i^2 + \frac{1}{\Lambda^4} \sum_{i,j,i<j} \tilde{\beta}_{ij} C_i C_j, \end{aligned} \tag{4}$$

where σ_{SM} is the SM cross-section for the given process and $\sigma_{\text{SM–EFT}}$ is an interference term between SM and BSM operators, which depends linearly on the Wilson coefficients C_i. The last term, $\sigma_{\text{EFT–EFT}}$, includes products of BSM operators, including possible interference between SMEFT operators, and depends quadratically on the Wilson coefficients C_i. The constants α_i, β_i, and $\tilde{\beta}_{ij}$ are used to parameterize the dependence of the cross-section on each Wilson coefficient. Their determination is described below.

For the presented results, the 'dim6top' model [51, 125] is used to implement SMEFT at leading order, using the Warsaw basis for the operators [126]. Signal events for this study were generated with the aMC@NLO MC generator and include contributions from the SM term, SM–EFT interference, and the EFT–EFT interference term. Within the dim6top model, there are numerous Wilson coefficients describing non-SM top-quark interactions. A total of 43 coefficients are systematically explored to identify those that could be constrained by the differential cross-section measurements.

Three different sets of operators are identified among these coefficients: 2-liqht-quark and 2-heavy-quark (2LQ2HQ) operators, 4-heavy-quark (4HQ) operators, and 2-heavy-quark plus boson (2HQV) operators. Measurements are made for a subset of coefficients, chosen with regard to sensitivity, stability of results for linear and linear+quadratic terms, and competitiveness with the results reported in global EFT fits [127, 128].

These sensitivity considerations lead to individual measurements of seven Wilson coefficients, all corresponding to 2LQ2HQ operators: $C_{Qq}^{3,8}$, $C_{Qq}^{1,8}$, C_{Qu}^{8}, C_{Qd}^{8}, C_{tq}^{8}, C_{tu}^{8}, and C_{td}^{8}. The operators feature different chiral and colour structures indicated by lower and upper indexes [51]. All these coefficients are purely real with no imaginary part. No individual limits are placed on 2HQV operators since the only sensitive coefficient, C_{tG}, does not provide limits competitive with the best one-dimensional limits available. However, the real part of C_{tG} is measured in combination with $C_{Qq}^{3,8}$ while no limit is placed

on the imaginary part of C_{tG}. No limits on 4HQ operators are presented since their sensitivity largely originates from terms in $\sigma_{\text{EFT–EFT}}$ suppressed by Λ^{-4}. As interference effects from dimension-8 operators with SM operators, for which no calculations are available, contribute to the cross-section at the same power of Λ, the interpretation of such limits is difficult. Simultaneous measurements of pairs of Wilson coefficients are made for three combinations that serve as an example for other combinations from the same set of operators. In particular, the measurement of C_{tG} vs $C_{Qq}^{3,8}$ is an example of the 2HQV vs 2LQ2HQ combinations and $C_{Qq}^{3,8}$ vs $C_{Qq}^{1,8}$ and $C_{Qq}^{1,8}$ vs C_{tq}^{8} are examples of 2LQ2HQ vs 2LQ2HQ combinations.

The differential cross-section at parton level as a function of $p_{\text{T}}^{t,1}$ is found to be more sensitive to EFT effects than the differential cross-sections for other observables ($|y^{t,1}|$, $H_{\text{T}}^{t\bar{t}}$, $m^{t\bar{t}}$, $\left|y^{t\bar{t}}\right|$) for which it is possible to make NNLO calculations using the Matrix program. EFT constraints are therefore set using the differential cross-section as a function of $p_{\text{T}}^{t,1}$. Tests were performed to verify that the unfolding procedure recovers within 1% the generator-level distribution for an input $p_{\text{T}}^{t,1}$ distribution that includes the EFT contributions for both $t\bar{t}$ signal and $t\bar{t}$ non-all-hadronic background where the Wilson coefficients values are set to the expected upper limits of this measurement.

For each bin of the $p_{\text{T}}^{t,1}$ distribution, a parameterization using the quadratic dependence of the differential cross-section as a function of a given Wilson coefficient is developed according to Eq. (4), i.e. the α_i, β_i constants for each Wilson coefficient and for each bin of the distribution are determined. The $\tilde{\beta}_{ij}$ constants are then estimated by fitting the above formula to samples having two C_i non-zero and using the previously determined values of α_i and β_i. The σ_{SM} parameter determined in the above parameterization gives the LO SM $t\bar{t}$ calculation and is not used.

The nominal Matrix NNLO calculation is employed as the SM prediction for the full model used to interpret the differential cross-section. The parameterization of LO EFT effects obtained above includes linear, quadratic, and cross-terms and is also used in the fit. The model includes all systematic and statistical uncertainties of the measurement, as well as their correlations as described by the covariance matrix of the differential measurement. In the model, the NNLO QCD scale uncertainty is used as a theoretical uncertainty and it is taken as fully correlated between the measurements. It was verified that a given scale variation always provides the maximum (or minimum) value for all the predictions. It was also verified that changing the correlation from 100% to 50% has little impact on the limits. The full fit is implemented in the Bayesian inference tool EFT*fitter* [129]. To make the dependence of the Wilson coefficients on the energy scale of the new physics explicit, the results are presented as the product $C_i(\text{TeV}/\Lambda)^2$. This also facilitates comparisons with other results where $\Lambda = 1$ TeV.

Fits of seven individual Wilson coefficients are performed with all other coefficients set to zero. A summary of the 95% confidence level (CL) and 68% CL limits is shown in Figure 34. The limits are provided for cases where both linear and quadratic terms are included and for cases where only linear terms are included. The 95% CL limits on $C_i(\text{TeV}/\Lambda)^2$ are within the range of $(-0.9, +0.5)$ for cases where both linear and quadratic terms are included. The inclusion of the quadratic terms leads to tighter bounds by 30%–60% for all Wilson coefficients. The ratios of various SMEFT predictions that include non-zero Wilson coefficients to the data for the leading top-quark $p_{\text{T}}^{t,1}$ distribution are shown in Figure 35. The effect of EFT contributions is seen mainly in the highest $p_{\text{T}}^{t,1}$ bin. Limits for selected pairs of Wilson coefficients are shown in Figure 36.

The 95% CL limit intervals for individual Wilson coefficients $C_{Qq}^{1,8}$, C_{tq}^{8}, and C_{tu}^{8} for cases where both linear and quadratic terms are included are about a factor of 4–5 smaller than those obtained from the measurement of the $t\bar{t}$ energy asymmetry [130]. Also, the 95% CL limits on individual Wilson coefficients

are typically 10%–50% more restrictive than the currently available individual limits from the global fits [127, 128].

The EFT analysis presented here shows that boosted $t\bar{t}$ differential cross-section measurements provide significant constraints on the SMEFT Wilson coefficients and can be used in global fits that include these top-quark Wilson coefficients.

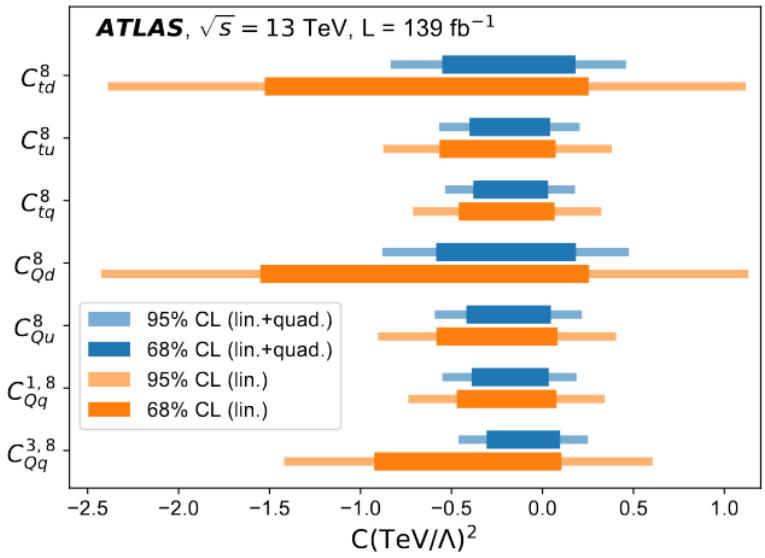

Figure 34: A summary of one-dimensional limits on selected Wilson coefficients corresponding to 2-light-quark 2-heavy-quark operators. The limits are provided for cases where both linear and quadratic terms are included and for cases where only linear terms are included.

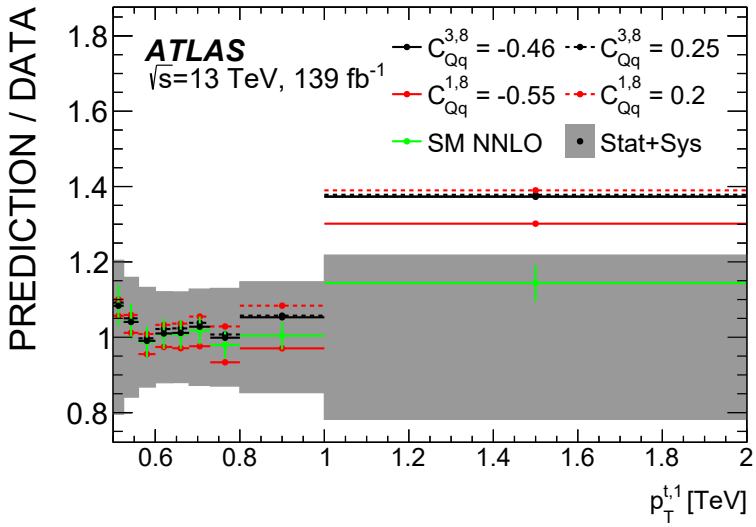

Figure 35: The ratio of various SMEFT predictions that include non-zero Wilson coefficients to the data for the leading top-quark $p_{\mathrm{T}}^{t,1}$ distribution. No uncertainties are included for these calculations. The values of non-zero Wilson coefficients correspond approximately to the 95% CL limits obtained by this measurement. The SM NNLO calculations as obtained by the nominal MATRIX settings is also shown. It includes the symmetrized scale uncertainty.